LAWRENCE
LIVERMORE
NATIONAL
LABORATORY

LLNL-TR-474338

On the Origin of Ultra High Energy Cosmic Rays II

T. K. Fowler, S. Colgate, H. Li, R. H. Bulmer, J. Pino

March 18, 2011

Disclaimer

This work performed under the auspices of the U.S. Department of Energy by Lawrence Livermore National Laboratory under Contract DE-AC52-07NA27344.

On the Origin of Ultra High Energy Cosmic Rays II

T. K Fowler[1], Stirling Colgate,[2] Hui Li[2] , R.H.Bulmer[3] and Jesse Pino[3]

[1]*University of California, Berkeley, CA 94720*

[2]*Los Alamos National Laboratory, Los Alamos, NM 87545*

[3]*Lawrence Livermore National Laboratory, CA 94550*

Abstract

We show that accretion disks around Active Galactic Nuclei (AGN's) could account for the enormous power in observed ultra high energy cosmic rays $\approx 10^{20}$ eV (UHE's). In our model, cosmic rays are produced by quasi-steady acceleration of ions in magnetic structures previously proposed to explain jets around Active Galactic Nuclei (AGN's) with supermassive black holes. Steady acceleration requires that an AGN accretion disk act as a dynamo, which we show to follow from a modified Standard Model in which the magnetic torque of the dynamo replaces viscosity as the dominant mechanism accounting for angular momentum conservation during accretion. A black hole of mass M_{BH} produces a steady dynamo voltage $V \propto \sqrt{M_{BH}}$ giving $V \approx 10^{20}$ volts for $M_{BH} \approx 10^{8}$ solar masses. The voltage V reappears as an inductive electric field at the advancing nose of a dynamo-driven jet, where plasma instability inherent in collisionless runaway acceleration allows ions to be steadily accelerated to energies $\approx V$, finally ejected as cosmic rays. Transient events can produce much higher energies. The predicted disk radiation is similar to the Standard Model. Unique predictions concern the remarkable collimation of jets and emissions from the jet/radiolobe structure. Given M_{BH} and the accretion rate, the model makes 7 predictions roughly consistent with data: (1) the jet length; (2) the jet radius; (3) the steady-state cosmic ray energy spectrum; (4) the maximum energy in this spectrum; (5) the UHE cosmic ray intensity on Earth; (6) electron synchrotron wavelengths; and (7) the power in synchrotron radiation. These qualitative successes motivate new computer simulations, experiments and data analysis to provide a quantitative verification of the model.

TABLE OF CONTENTS

1. Introduction

This paper builds on Ref. [1] in which it was hypothesized that ultra high energy cosmic rays $\approx 10^{20}$ eV (UHE's) arise as electric currents created by Active Galactic Nuclei (AGN's). Accumulating evidence supports this hypothesis. Only the gravitational energy of supermassive black holes inside AGN's could sustain the enormous power in the measured cosmic ray energy spectrum for the duration of radiolobes $\tau \approx 10^8$ yrs, yielding 10^{60} ergs per galaxy spacing volume [1]. Synchrotron radiation from jets creating radiolobes indicates the presence of strong magnetic fields [2]. New experimental evidence supports the contention that an AGN accretion disk can act as a dynamo [3]. Direct attempts to correlate UHE's with known AGN's are limited by statistics but may yet pin down UHE origins [4].

As further support for the cosmic ray hypothesis of Ref. [1], this paper presents a new model of cosmic ray acceleration by AGN's producing a dynamo. In our model, the dynamo voltage V ejects a steady current I, mainly in a central column where most of the gravitational power is deposited (see sketch in Figure 1). At the advancing "nose" in Figure 1, where the current begins its return to the disk, the voltage V reappears as the inductive electric field that causes ions to "stick" to advancing field lines. The inductive field also accelerates ions radially to produce UHE cosmic rays if there exists a turbulent diffusion coefficient D driving ion current perpendicular to magnetic field lines. The required $D \approx r_{Li}\omega_{Ci}$ (ion Larmor radius r_{Li}, cyclotron frequency ω_{Ci}) is shown to arise naturally from electrostatic instability of the non-Maxwellian ion distribution created by runaway acceleration of the ions.

Secondary themes of the paper, adding credibility to the cosmic ray acceleration model, are: (a) mechanisms creating a dynamo by accretion from an external reservoir [5], as in Figure 1; (b) the role of jet ejection in recycling essentially all of the angular momentum entering the dynamo back to the reservoir via the jet and its return current, giving an accretion model considerably different from the "Standard Model" discussed in Ref. [2]; and (c) the diffuse pinch current outside the main jet column in Figure 1, whose stability properties account for collimation over the observed jet length L, and the formation of radiolobes at the end of the jet.

As with many earlier efforts, our model treats dynamics as a succession of quasi-equilibria, in our case justified by the slow rate of expansion of the jet compared to Alfven speeds governing plasma motion. We are looking at a quasi-steady "snapshot" toward the end of this process. Like all "Poynting" models, we must assume the existence of coherent magnetic fields when a dynamo is created by accretion, justified by experiments and computer modeling demonstrating the growth of coherent fields.

What appears to be new is that, given a coherent field, the conservation of canonical angular momentum of ions accreting in this field becomes the governing mechanism that both gets rid of all excess angular momentum as found by other authors, and also introduces several simplifications allowing a complete analytical solution for disk and jet parameters. We obtain quasi-steady radial profiles for 7 accretion disk variables: the line density, the disk height, the surface temperature, the accretion velocity, the disk rotation frequency, the dynamo poloidal magnetic field, and the dynamo current. Also the jet magnetic field and current profiles, which match those of the disk.

The predicted disk temperature and radiation are similar to the Standard Model. The unique predictions concern the jet and emissions from the jet/radiolobe structure. With just the 2 inputs of the Standard Model – the black hole mass and the accretion rate – the model makes 7 predictions roughly consistent with data: (1) the jet length; (2) the jet radius; (3) the steady-state cosmic ray energy spectrum; (4) the maximum energy in this spectrum; (5) the UHE cosmic ray intensity on Earth; (6) electron synchrotron wavelengths; and (7) the power in synchrotron radiation.

The paper is organized as follows. The magnetic accelerator structure is discussed in Section 2, cosmic ray acceleration in Section 3, the cosmic ray energy spectrum in Section 4, other model predictions and signatures including jet collimation, radiolobe formation and synchrotron radiation in Section 5, and a summary of results in Section 6. To maintain narrative flow, detailed discussions of magnetized accretion disks creating dynamos are given in Appendices. Appendix A develops an accretion model with strong magnetic fields; Appendix B derives the magnetic profiles of Figure 1, using this model; and Appendix C discusses transport by the magneto-rotational instability essential to the model. More details are given in Ref. [6].

We use cylindrical coordinates r, ϕ, z fixed in the black hole, with z along the axis of rotation of the accretion disk. Except as noted, units are cgs, often introducing c, the speed of light.

2. Accelerator Structure

Figure 1 closely resembles "spheromak" plasmas created in the laboratory [1]. To understand astrophysical spheromaks, imagine a conducting disk connected by a shaft to a source of rotation, with coils generating a poloidal magnetic field B_z perpendicular to the disk. Let this assembly rotating at angular frequency Ω be mounted at one end of a metal chamber, as in Figure 2. If the chamber were evacuated, in the laboratory reference frame rotation would produce surface charge so that the disk acts as a capacitor with electrostatic field $E_r = c^{-1} r\Omega B_z$ across the face of the disk. Gas supplied to the disk would break down to create a fully ionized plasma ejected from the disk.

As discussed in Ref. [7], the homopolar generator in Figure 2 is identical with actual experiments creating "spheromaks" in which a capacitor-driven plasma gun replaces the generator. Spheromak experiments for magnetic fusion research inject current into a metal chamber for a time long compared to transit times across the chamber, with the goal of building up magnetic fields inside the chamber to values sufficient to confine high temperature plasmas [8]. Experiments devoted to astrophysics may focus on the formation and ejection of jets resembling the astrophysical structures in Figure 1[9].

Here we will model the final stage of AGN accretion and jet ejection keeping in mind lessons from laboratory experiments and computer simulations of these experiments, and recent simulations of astrophysical jets discussed below [10]. As in the Standard Model mentioned in the Introduction, we treat the final stage of accretion as a quasi-steady state in which dynamo properties are fixed, while the jet length L continues to expand. The main difference from the Standard Model is the dominant role of magnetic torque ejecting disk angular momentum into the jet, as in Ref. [11], whereas in the Standard Model all angular momentum is dissipated by a viscosity of uncertain origin [2]. In Appendix A, we provide a self-consistent estimate of the accretion velocity v_r and other relevant quantities yielding a sustained dynamo.

We are primarily interested in features of the magnetic structure leading to ion acceleration. Since initially ions ejected from the disk follow magnetic field lines, the initial stage of acceleration requires $\mathbf{E}_{||}$ parallel to **B**, forbidden by the ideal Ohm's Law but made possible by MHD turbulence in the central column of Figure 1, producing $\mathbf{E}_{||}$ parallel to the symmetrically-averaged mean magnetic field. However, as discussed in Section 3, $\mathbf{E}_{||}$ acceleration in the central column is limited by ion synchrotron radiation and cannot achieve the enormous energy of UHE's. The final stage of acceleration to UHE energies turns out to be driven by the large inductive electric field in the advancing nose, requiring acceleration perpendicular to field lines due to a non-MHD plasma turbulence process inherent in the runaway ion beam emerging from the central column. Thus explaining UHE's reduces to calculating the inductive electric field in the nose.

In this section, we are mainly concerned with the central column of Figure 1, where magnetic relaxation by internal kink modes extending into the disk, discussed in Appendix B, can lead to a relaxed magnetic field with known profiles, hence describable by a 0-D model with the radius a, poloidal field B_o and current I as parameters. The system evolution in time is dominated by inductance, the jet mass density being very low, just that needed to carry current ejected by an electrostatic sheath that forms at the disk surface at a location where the sheath voltage equals the energy required to escape gravity [6]. If collisions are negligible in the sheath, for a positively-charged disk the sheath current is a "runaway" ion beam with density n_i given by:

$$n_i = (I/e\langle v\rangle A) \qquad (1)$$

where $\langle v\rangle$ is the average ion speed carrying the current ($\rightarrow$ c, the speed of light) and A the cross-sectional area. If collisions remain negligible in the jet, the runaway ion beam continues to carry the current in the jet, since relativistic electron (or electron-positron) current tends to be canceled in our fixed reference frame centered on the black hole, due to two-stream instability [6,12,13]. Higher density in laboratory jets is due to gas sources beyond the sheath. Such sources are largely absent in an AGN jet (see Appendix B), and hydrodynamic jets that might add to gas loading from the disk are likely to polarize and

pass through the current jet without adding to its mass [6]. The exact ion density does not matter for our purposes, as long as collisions are too weak to inhibit ion acceleration.

Inductance-dominated jet/radiolobe dynamics is described by:

$$d/dt\ (1/2\ I^2\Lambda) = IV - \int dx\ \mathbf{j}\cdot\mathbf{E} \approx (1 - \alpha_{ACCEL})\ IV \qquad (2)$$

$$V = - c^{-1}\ a\Omega(a)\ aB_o \qquad (3)$$

where $\Lambda \propto L$ is the jet/radiolobe inductance with jet length L and $V = aE_r$ with E_r above. In Eq. (2), $\int dx\ \mathbf{j}\cdot\mathbf{E}$ is dissipation by ion and electron acceleration, parametrized as $\alpha_{ACCEL}(IV)$. In Eq. (3), the minus sign follows from negative rotational velocity $v_\phi = r\Omega$ to yield positive B_ϕ for positive B_z.

Next we note that I saturates at a constant value, verified below. For a chamber of finite length, I grows until limited by dissipation in the plasma [14]. In unbounded space, L grows while I saturates when $B_\phi = (2I/ca)$ first equals B_z near the black hole, giving:

$$I = (c/2)\ aB_o \qquad (4)$$

Eq. (4), which was verified in the simulations in Ref. [10], is known in the laboratory as "bubbleburst," occurring when current is first ejected from a magnetized plasma gun.

It remains to calculate the inductance Λ, and from this the inductive electric field at the nose. To calculate Λ, we note that in quasi-steady state the magnetic field of the jet is independent of time except at the advancing nose. Since current is concentrated in the central column, in the diffuse pinch we expect $B_\phi(r) \approx (2I/cr)$, while B_z is determined by maching $B_z(r)$ in the jet with that in the dynamo. At large r, B_z in the dynamo is determined by the conservation of canonical angular momentum of falling ions. For constant canonical angular momentum $P_\phi = (m_i r^2\Omega + erA_\phi)$ with ion charge e, mass m_i and vector potential A_ϕ, taking $\partial P_\phi/\partial r = 0$ yields:

$$B_z = r^{-1}\ \partial(rA_\phi/\partial r) = - (m_i/e)\ r^{-1}\ \partial(r^2\Omega)/\partial r \qquad (5)$$

Eq. (5) is a robust result implying the dominance of dynamo torque over viscosity in accounting for angular momentum conservation, leading to the angular momentum equation of our modified Standard Model of accretion in Appendix A. Eq. (5) fails only if there exists a competitive viscosity with a "collision" frequency greater than the poloidal cyclotron frequency, not likely and not true for the Standard Model, which postulates a viscosity corresponding to a collision frequency c_S/H for sound speed c_S and disk height H [2].

Like the Standard Model, we make the thin-disk approximation, by integrating 2D equations over the disk height. Then we can take $B_r = 0$ inside the disk whereby the dynamo field matches onto a force-free jet having the same $B_z(r)$, $B_\phi(r)$ as those at the dynamo/jet interface. In Appendix A, we show that $\Omega \propto (a/r)^{3/2}$ (Keplerian scaling) giving, by Eq. (5), $B_z(r) \propto \Omega \propto (a/r)^{3/2}$ at large r, while the toroidal component $B_\phi(r) \approx (2I/cr) \propto 1/r$. Applied to the jet, this shows that B_ϕ dominates the inductance, giving:

$$\Lambda \quad = \quad \int_0^R 2\pi L r dr\, [(B_z^2 + B_\phi^2)/8\pi]/(I^2/2) \approx \quad L[2\ln(R/a)/c^2] \qquad (6)$$

whereby, for constant I, Eqs. (2) - (4) give:

$$dL/dt \quad = \quad (1 - \alpha_{ACCEL})(V/I)[c^2/\ln(R/a)] \; = 2(1 - \alpha_{ACCEL})[(-a\Omega)/\ln(R/a)] \qquad (7)$$

$$L \quad = \quad 2(1 - \alpha_{ACCEL})(-a\Omega\tau/\ln(R/a)) \quad \approx \quad (-a\Omega\tau/\ln(R/a)) \qquad (8)$$

where R is the radiolobe radius in Figure 1.

By Eq. (8), $L \rightarrow 0$ as $\alpha_{ACCEL} \rightarrow 1$, indicating that 100% efficient acceleration would leave little excess energy stored as the magnetic energy of the jet/radiolobe structure. In Ref. [6], we argue that $\alpha_{ACCEL} \approx 1/2$, giving L on the far right in Eq. (8). Then half of the $IV\tau$ is stored as magnetic energy at the nominal end of life of the system of duration τ. By Lenz's Law, this stored magnetic energy would continue to drive acceleration as the field decays, eventually dissipating all of $IV\tau$, mainly as cosmic rays as we shall see.

This simple model is confirmed by Figures 3 and 4 discussed in Appendix B and by MHD simulations in Figure 5. Fig. 5a gives the 2D mean field similar to Figure 1; in Fig. 5b, the actual 3D field from which this mean field was constructed; and in Fig. 5c the dominant $B_\phi(r) \propto 1/r$ despite weak instability partially filling the volume between the central column and the return current [10]. By Eq. (6), the inductance is dominated by the large volume of the radiolobe, with radius R occurring where $(B_\phi(R)^2/8\pi) = p_{AMB}$, the ambient pressure [10, 15, 16]. Typically, we will find $\ln R/a \approx 20$, giving a significant slowing of the jet expansion as is needed to account for observed lengths $L \approx 10^{24}$ cm $\approx$ 1 Mpc [1, 2, 6]. Why kink instability is weak outside the central column is discussed in Sections 3 and 5, and Appendix B.

To determine the inductive electric field accelerating cosmic ray ions in the nose, we note that radial hoop forces in the nose $\propto \nabla B^2$ compete with length expansion to create a blunt nose, as shown in Figure 1, discussed in Appendix B and verified in Figure 5a. Then field lines are nearly radial, giving nose forward motion $v_z(r) \approx dL/dt$ approximately independent of r, giving $E_r = c^{-1}v_z B_\phi = C/r$. Since we will find little voltage drop along the central column, most of the voltage reappears at the nose, giving $V = \int_a^R dr\, E_r = C \ln R/a$, hence $C = V/\ln R/a$ and:

$$E_r = (V/r \ln R/a) \tag{9}$$

Given $v_z(r) = dL/dt$ independent of r (a 1D problem), we can show why the current hovers around the "bubbleburst" value, Eq. (4), using Eq. (2) and a simplified 1D equation for the ion dynamics:

$$\rho\, dv_z/dt = \rho(d^2L/dt^2) = c^{-1} j_r B_\phi \tag{10}$$

Substituting $B_\phi = (2I/cr)$ and $\rho = (j_r/ec)m_i$ from Eq. (1) gives:

$$(m_i/e)\, d^2L/dt^2 = (2I/cr) \tag{11}$$

Always I cannot be less than that in Eq. (4), this being the condition for current ejection. With this constraint, numerical solutions of Eqs. (2) and (11) show that, starting from this minimum value of I, dL/dt grows rapidly by Eq. (11), which for constant V causes I to fall by Eq. (2) [6]. Since this would disrupt the jet, I hovers at the value in Eq. (4) and dL/dt satisfies Eq. (2) with $dI/dt \approx 0$ and Λ in Eq. (6), giving Eq. (8). See Appendix B for the 2D version of this proof.

We conclude this section with example values of a, B_o and Ω appearing in Eqs. (3) and (4), to be used to evaluate quantities in later sections. We require both a mass and a time scale, for which we take a typical AGN black hole mass $M_{BH} = 2 \times 10^{41}$ gms equal to 10^8 Sun masses and a lifetime $\tau = 10^8$ yrs $= 3 \times 10^{15}$ sec typical of jet/radiolobes for a range of black hole masses [1, 2]. Results are insensitive to the radiolobe radius R. As noted above, we take constant R giving ln R/a = 20, and, anticipating results of Appendix A, we assume $a \approx 10\ R_G$ (with $R_G = 2\ M_{BH}G/c^2$ for Newtonian gravitational constant G). Finally, we set $IV = f(1/2M^*c^2) = f(3 \times 10^{46}$ erg/s) with $M^* \equiv M_{BH}/\tau$, f being the estimated efficiency of converting gravitational power $(1/2M^*c^2)$ into magnetic energy. Taking f = 0.25 (25%) as estimated in Appendix A, we obtain, with Keplerian - $\Omega = (M_{BH}G/a^3)^{1/2}$ and using Eqs. (3), (4) and (8):

a	=	3×10^{14}	cm	(12)
$a\Omega$	=	- 0.2 c		
B_o	=	5×10^3	gauss	
V	=	9×10^{19}	volts	
I	=	7×10^{18}	amps	
L	=	10^{24}	cm	

where B_0 is an average value of B_z inside the central column. Parameters for other values of M_{BH} can be obtained by scaling, giving for fixed τ , fixed a/R_G, fixed $a\Omega/c$ and fixed efficiency, $IV \propto (aB_o)^2 \propto M_{BH}$, hence $a \propto M_{BH}$ and $B_o \propto M_{BH}^{-1/2}$ and $I \propto V \propto M_{BH}^{1/2}$.

The efficiency f could be greater inside the central column, which receives a fraction $(1 - R_G/2a)$ (95%) of the gravitational energy. Energy not converted to IV or radiation flows into the black hole, perhaps producing still more current and IV power, as

in Ref. [11]. In Section 3, we will conclude that only 5% of the IV power in the central column produces synchrotron radiation, the rest being ejected as cosmic rays in the nose, both in quasi-steady state and during the decay of the stored magnetic energy as noted above.

3. Cosmic Ray Acceleration

Next we discuss how the accelerator structure of Section 2 might produce UHE cosmic rays. Briefly, cosmic rays are created by the dynamo-driven jet/radiolobe structure because the jet density in Eq. (1) is so low that collisions are irrelevant, thus allowing accelerated ions to run away to high energies.

As in Section 2, we will assume a voltage polarity accelerating ions out of the disk into the central column of Fig. 1. For the quadrupole field of Refs. [17] and [18], the polarity is the same for both sides of a two-sided pair of jets. The opposite polarity gives similar results, with a "virtual" anode injecting ions into the nose [6].

We begin our discussion of ion acceleration by considering magnetic relaxation due to MHD instability of current due to internal kink modes, discussed in Section 5 and Appendix B. As is well known from theory confirmed by simulations [19], a 3D magnetic perturbation $\delta\mathbf{B}$ of the 2D mean field (averaged over ϕ) creates an electric field parallel to the mean field, given by [6, 19]:

$$E_{||} \approx (v_o B/c)(<\delta B^2>/B^2) < (a/ct)B_o \qquad (13)$$

where δB^2 is appropriately averaged over time and $v_o < v_A$, the Alfven speed. Eq. (13) represents magnetic relaxation by hyper-resistive current diffusion [6,14], giving in the middle expression $E_{||} = \eta_H j_{||} \equiv c^{-1}(DB/a)$ with $D = (c^2\eta_H/4\pi) = v_o a(<\delta B^2>/B^2)$. That instability occurs only inside the central column is shown in Appendix B. That magnetic relaxation is very limited in expanding jets, giving the bound on the right hand side of Eq. (13), comes from the following quasi-linear estimate of D, whereby the free energy driving instability is due to diffusion D spreading the central column current channel to a radius $R_1 = \sqrt{(a^2 + Dt)}$ [6]. The free energy arises from a slight increase in B (and I) above the bubbleburst value B_o in Section 2 [14]. Then energy conservation (per unit length)

requires $B^2a^2 = [B_o^2 + <\delta B^2>)]R_1^2$. Dividing by B^2a^2 and replacing $<\delta B^2> = D(B^2/v_oa)$, we obtain an equation for D:

$$1 \quad = \quad [(B_0^2/B^2) + (Dt/a^2)(a/v_ot)][1 + (Dt/a^2)] \qquad (14)$$

with $B_0^2/B^2 < 1$. For $t \approx \tau$ in steady state, we can assume $(a/v_ot) << 1$, giving $(Dt/a^2) \approx [1 - (B_0^2/B^2)] < 1$ independent of v_o and from this $<\delta B^2>/B^2 = (D/v_oa) < (a/v_ot)$ which gives the right hand side of Eq. (13). For $v_o \approx c$ and $t \approx \tau$, $\delta B/B \approx 10^{-6}$ for numbers in Eq. (12).

Eq. (13), together with Eq. (8), gives:

$$\Delta V \quad = \quad LE_{||} \quad < \quad (-a\Omega t/\ln(R/a))(a/ct)B_o = \quad (V/\ln(R/a)) \qquad (15)$$

This ΔV could accelerate ions to high energies in the central column. However, actually the energy saturates when $ecE_{||} = 2/3\ (e^2\alpha^2\gamma^4/c^3)$ [20], the synchrotron radiation with $\alpha = c^2/R_C$ for ions following field lines with curvature radius R_C, giving for rest mass energy γ:

$$\gamma \quad \leq \quad (3/2\ E_{||}R_C^2/e)^{1/4} \qquad (16)$$

For numbers in Eq. (12), and using $E_{||} = \Delta V/L$ in the central column, this limits the energy of ions entering the nose to $\gamma \approx 10^7$ (10^{16} eV), far below $\gamma > 10^{10}$ for UHE's.

As field lines spread out in the nose (where $R_C \approx r$), synchrotron radiation diminishes, giving finally ion orbits with Larmor radii equal to the current channel thickness $\Delta \approx a$ [6]. Then ions escape too soon, unless the flux width Δ expands to contain the ions. That Δ probably does expand, due to ion pressure, can be seen as follows. Due to synchrotron radiation, ions lose energy until a further loss of $v_\perp$ perpendicular to **B** would cause the ions to leave the field lines. Then the ion beam pressure perpendicular to **B** tends to be just that corresponding to the minimum $v_\perp$ necessary for ions to follow curved field lines, yielding $\beta_\perp$ (pressure perpendicular to **B** in ratio to magnetic energy) given by:

$$\beta_\perp \text{ (nose)} \quad = \quad (8\pi n_i m_i \gamma v_\perp^2/B_\phi^2) \quad = \quad 2(v_\perp/\langle v\rangle)(r_L/\Delta) \qquad (17)$$

where we use $n_i = (I/e\langle v\rangle A)$ from Eq. (1) with $A = 2\pi\Delta r$ in the radially fanning return current channel in the nose, with width Δ; $B_\phi = B_o(a_o/r)$ for B_o in the central column; and Larmor radius $r_L = (m\gamma c v_\perp/eB_\phi)$. As $r_L \rightarrow \Delta$, the tendency to escape also gives $v_\perp \rightarrow \langle v\rangle \approx c$ so $\beta_\perp \rightarrow 1$. Then the field is no longer force free; Δ grows with r_L; and the poloidal flux expands, leaving B_ϕ as the dominant field component. Since the current flows radially in the nose, the current must flow perpendicular to B_ϕ. This requires some kind of turbulent diffusion, giving:

$$(j_r)_{NOSE} \quad = \quad - eD_{DC}\,(dn_i/dr) \qquad (18)$$

The necessary diffusion can arise from a known instability of the ion beam, the non-MHD electrostatic "drift cyclotron" (DCLC) instability derived from kinetic theory [21]. This instability is resonant with ions only and acts like an ion "collision" causing diffusion in space and energy [22]. The expected quasi-steady diffusion rate is [6]:

$$D_{DC} \quad \approx \quad cr_L \quad \text{if} \quad |r_L n^{-1}\nabla n| \;=\; (r_L/\Delta) > 0.4(2v_\perp^2/c^2\beta_\perp)^{2/3} \qquad (19)$$

The instability condition on the right is derived from $r_L/\Delta \geq 0.4(\omega_C^2/\omega_P^2)^{2/3}$ with relativistic ion cyclotron frequency ω_C and relativistic ion plasma frequency ω_p [Eq. (148) of Ref. [21]]. As $r_L \rightarrow \Delta$ and ions try to escape, $v_\perp \rightarrow \langle v\rangle \approx c$ as noted above, and $\beta_\perp \rightarrow 1$ by Eq. (17). Thus, just in time, the instability condition needed to sustain the current is satisfied.

The radial current j_r represents a new kind of quasi-steady ion acceleration, in which the power j_rE_r is provided by the steady inductive electric field E_r in the nose (Eq. (9)). Related ideas are discussed in Ref. [23].

We conclude this section with a comment on the ratio ($\int d\mathbf{x}\, \mathbf{j}\cdot\mathbf{E}$ /IV) approximated as 1/2 in Eq. (8). Since the dominant dissipation is due to cosmic rays generated in the nose, the factor 1/2 is a measure of where DCLC acceleration commences along the

voltage drop V over a < r < R. This issue is explored in some detail in Ref. [6] with the conclusion that 1/2 is a reasonable estimate.

4. Cosmic Ray Energy Spectrum

To calculate the quasi-steady cosmic ray intensities, we note that DCLC instability causes leakage across the current channel at about the same diffusion rate as that driving the current [6, 22]. The cosmic ray energy distribution N(E) is given by:

$$N(E) \;=\; \int_a^R dr \int_0^H dz\, (-D\, \partial^2 F(r,z,E)/\partial z^2) \;=\; \int_{R(E)}^R dr\, (I/e\langle v\rangle)\, f(E)\, (\kappa^* D/\Delta^2) \quad (20)$$

where $F(r,z,E) \approx n(r,z)f(E)$ is the ion Vlasov distribution function with variables r, z and ion energy E. In the second step we approximate $\int dzn = (I/e\langle v\rangle)$, the line density from Eq. (1), and $\partial^2/\partial z^2 \approx \kappa^*/\Delta^2$ with dimensionless factor κ^* to be adjusted to insure energy conservation. We approximate the time-averaged ion energy distribution f(E) due to drift cyclotron diffusion downward in energy by constant $f(E) = E(r)^{-1}$ over $0 < E < E(r)$, $E(r) = \int_a^r dr\, E_r = e(V/\ln R/a)\ln(r/a)$ being the maximum energy at r due to acceleration by E_r in Eq. (9). There are no ions with energies > E(r) at r, giving as the correct lower limit of integration R(E), the smallest radius at which E(r) > E. Changing variables from r to E(r) gives $dr = d(E(r))[r \ln(R/a)/eV]$. Also we approximate $\langle v\rangle = D/r$ and we take $\Delta \approx r_L$ in the nose, as argued in Section 3, giving $\Delta(r) = (m_i\gamma c v_\perp/eB_\phi) \approx r(E(r)/5eV)$ using $B_\phi = B_o(a/r) = 0.2(V/cr)$ by Eq. (3). Then r's and D's cancel, giving:

$$\begin{aligned} N(E) \quad &\approx \quad (I/e)\,[\kappa^*\, 25 \ln(R/a)] \int_E^{eV} dE(r)(eV/E(r)^2)\, f(E) \\ &= \quad (I/e)[\kappa(eV)^{\Gamma-1}]\, E^{-\Gamma} \quad , \qquad \Gamma = 1+k \end{aligned} \quad (21)$$

where κ absorbs κ^* and other numerical factors. For $f(E) = E(r)^{-1}$, the integral yields k = 1 giving $\Gamma = 2$. Setting k = 1.7 gives the measured value $\Gamma = 2.7$, implying some deviation from f(E); kinetic simulations could determine f(E) and k.

The observed intensity is $(1/km^2\ yr)$ at energies > 10^{19} electron volts $\equiv E_1$, from 472 sources < 240 Mlyr away [4]. For spherically uniform sources within R_C = 240 Mlyr, this implies an average source density S satisfying $\int_0^{Rc} 4\pi r^2 dr(S/4\pi r^2) = SR_C = (1/km^2\ yr)$,

giving a total source strength $I_S = \int_0^{Rc} 4\pi r^2 dr S = 2 \times 10^{17}$ amps for hydrogen. We found in Section 2 that a single cosmic ray source with $M_{BH} = 10^8 M_{SUN}$ yields 7×10^{18} amps, but not all at energies capable of reaching Earth. The fraction I_{19} above energy E_1 is:

$$I_{19} = \int_{E1}^{eV} dE\, N(E) = I\,(\kappa/1.7)[(eV/E_1)^{1.7} - 1] \leq 2 \times 10^{17} \text{ amps} \quad (22)$$

where $V = 9 \times 10^{19}$ volts and $I = 7 \times 10^{18}$ amps from Eq. (12), and the adjustable parameter $\kappa = 1.2 \times 10^{-3}$ to satisfy $\int d\mathbf{x}\, \mathbf{j}\cdot\mathbf{E} = 1/2\, IV = \int_{E2}^{eV} dE\, EN(E)$ (by Eq. (2)) for $E_2 = 10^{16}$ electron volts entering the nose ($\gamma \approx 10^7$ by Eq. (16)). While not all AGN's produce jets [2], we see that just a few massive black holes with jets could account for observed UHE cosmic ray intensities, and the dynamo voltage $V \approx 10^{20}$ volts by Eq. (12) accounts for maximum energies in the quasi-steady spectrum [1].

Transients for times $t << \tau$ in Eq. (13) could account for a few cosmic rays >> 10^{20} eV [1,6]. Such transients would represent a local, rapid injection of helicity into the lobe(s), forbidden on average by the tendency of the current to hover at the current given by Eq. (4), as discussed in Section 4. Then transients at speed $\approx c$ only recur after a time sufficient to replenish the energy, giving a duty cycle $\approx c^{-1}(dL/dt) \approx 1\%$, hence an intensity much lower than the quasi-steady intensity of Eq. (21).

Note that ion losses discussed above must be made consistent with retaining a supply of hot ion current carriers and sufficient electrons to neutralize space charge. This is accomplished by inward transport recycling plasma from the ambient pressure wall pushed ahead of the nose. Transport includes magnetic drifts mentioned in Appendix B that add to DCLC losses. However, whereas magnetic drifts only act to eject hot ions, DCLC spatial transport out of the nose is due to turbulent **E** x **B** drifts acting equally on all ions and electrons [21, 22]. Thus DCLC transport $-D\partial F(\mathbf{x},\mathbf{v})/\partial z$ for ions and for electrons can both maintain current carriers and charge neutrality through differences in $\partial F(\mathbf{x},\mathbf{v})/\partial z$, which can be positive for the cold ambient ions and electrons in the distribution but just enough negative for hot ions to do in detail what adjusting κ does in our model. This implies recycling of cold ions from the ambient pressure wall being pushed ahead by the jet, giving a recycling rate $I_{RECYCLE} = \int_{E2}^{eV} dE\, N(E) > 1000\, I$.

5. Jet Collimation, Radiolobes, Electron Synchrotron Radiation

As derived in the Appendices, black body radiation from the accretion disk would be similar to that derived from the Standard Model, in agreement with data [2, 24]. The main difference in our model is that radiation is weaker than the Poynting vector power at large r but becomes comparable to Poynting power as $r \rightarrow a$, disk radiation then accounting for about 25% of the 95% of the gravitational power that enters the central column. A fixed 25% of the gravitational power in radiation could in fact determine the lifetime $\tau \approx 10^8$ yrs otherwise taken as an input parameter in our calculations. In our model, the portion of the disk at $r < a$ radiates as an approximate sphere of radius a, subject to the Eddington limit on the lifetime given by:

$$\tau \approx 0.25\ (.95)(1/2\ M_{BH}c^2/L_{EDD}) = 1.6 \times 10^{15} \approx 10^8\ \text{yrs} \qquad (23)$$

where $L_{EDD} = 1.3 \times 10^5\ M_{BH}$ giving τ independent of M_{BH} as observed [1,2]. With this interpretation, our quasi-steady snapshot of an accretion dynamo, in Appendix A, is the final stage of a process that burns itself out in a time τ, at an ever faster accretion velocity near the black hole that prevents replenishing the dynamo after that time.

The unique predictions of our model concern emissions from the highly visible jet/radiolobe structure. Note that the cosmic ray acceleration model of Sections 2-4 is independent of the jet length L. Yet the most striking feature of AGN jets is their apparent collimation over a very long length L before radiolobes form, despite the well-known tendency of current columns to undergo "kink" modes such as those observed in Fig. 5b [25]. As it turns out, the long length is probably due to the well-known stabilizing effects of the diffuse pinch in Figure 1, though the diffuse pinch has negligible effect on cosmic ray acceleration.

Kink modes can be divided into internal modes and external modes. Internal modes, discussed in Appendix B, are mainly important in driving $E_{||}$ in the central column, Eq. (13). External modes are rigid motions of the entire current profile, potentially destroying collimation, described by 3D perturbations around the mean magnetic field **B** given by $\delta\mathbf{B} = \nabla \times (\boldsymbol{\xi} \times \mathbf{B}) \propto \exp i(m\phi + 2\pi nz/L)$ for a radial displacement $\boldsymbol{\xi}$ of the current boundary of a diffuse pinch of length L. Instability occurs

if the external mode free energy δW is negative, requiring, for a pinch isolated from nearby walls, qn < 1 with q defined below. This condition is always satisfied for a long diffuse pinch surrounded by a vacuum or a plasma that is too resistive or too low in density to support the currents implied by δ**B**, but the corresponding δW can be very small. Shafranov derived an approximate formula for δW for a diffuse pinch, giving stability for m ≥ 2, and for the most unstable case with m = 1 [25]:

$$\delta W_{KINK} = - L\xi^2 B_\phi(R_o)^2\, qn(1 - qn), \quad q = (2\pi R_o/L)(B_z/B_\phi)_{Ro} \qquad (24)$$

where R_o is the diffuse pinch radius in Figure 1.

The assumed large radial extent of the diffuse pinch current, supported by our discussion of radial magnetic profiles in Appendix B, may explain the collimation of the jet. Radiolobes are likely to form where magnetic perturbations of the diffuse current jet first grow to appreciable amplitude. The criterion of Eq. (24) gives instability if qn < 1 where, for the diffuse pinch profile of Appendix B ($B_\phi \propto (a/r)$ and $B_z \propto (a/r)^{3/2}$), we obtain:

$$q_{Ro} = (2\pi R_o/L)(B_z(R_o)/B_\phi(R_o)) = (2\pi R_o/L)(a/R_o)^{1/2} \qquad (25)$$

This always gives instability for a long pinch, but with weak free energy, δW. The only unstable external modes are rigid displacements (constant radial ξ_r, azimuthal m = 1, axial mode number n), with growth rate γ_{KINK} given by [25]:

$$\gamma_{KINK} = [- \delta W/\int 2\pi r dr dz \xi^2 \rho]^{1/2} \approx 2\,(c/R_o)\,(nq_{Ro})^{1/2} \qquad (26)$$

To obtain the expression on the right, we note that the kink mode probably terminates at the electrostatic sheath at z = H, giving $\int 2\pi r dr dz \xi^2 \rho \approx \xi^2 L \pi a^2 \rho(a)$, and we use $\delta W = - \xi^2 L q_{Ro} n B_\phi(R_o)^2$ from Eq. (24). Then, using $B_\phi(R_o)^2 = B_o^2(a/R_0)^2$, the ratio in […] in the middle expression becomes $(B_\phi(R_o)^2/\pi a^2\rho(a))(nq_{Ro}) = 4(v_A(a)/R_0)^2(nq_{Ro}) = 4(c/R_0)^2(nq_{Ro})$ for the low density of the central column.

Despite kinking, the jet would retain the good collimation derived in Appendix B up to the nose which experiences the maximum number of growth periods $\gamma_{KIN}\tau$, typically requiring 20 or more growth periods to create radiolobes out of noise at the nose. For q_{Ro} from Eq. (23) and $B_\phi(R_o) = B_o(a/R_o)$ and $B_z(R_o) = B_o(a/R_o)^{3/2}$, we obtain:

$$\gamma_{KINK}\tau \quad = \quad 2\,(c\tau/R_o)\,[(2\pi\, R_o/L)(a/R_o)^{1/2}]^{1/2} \quad \approx \quad 50 \qquad (27)$$

where we take n = 1 for kink modes with wavelength ≈ L; $c\tau/R_o = 10^{4}$, $R_o/L = 10^{-2}$ and $(a/R_o) = 10^{-8}$ for R_o below and a in Eq. (12). Higher n modes may affect structure along the jet.

In Appendix B, we show that the diffuse pinch joins smoothly onto the disk so that the diffuse pinch radius R_o is also the O-point radius of the dynamo where B_z and j_z change sign, hence the boundary of power supplied to the jet. Also the O-point radius is effectively the edge of the accretion-sustained dynamo, which grows radially until the gravitational energy is exhausted, by jet ejection, disk radiation and energy falling into the black hole – all estimated in Appendix A. Then, for the accretion velocity $v_r = r(MG/r^3)^{1/2}$ in Appendix A, Eq. (A19b), we estimate for numbers in Eq. (12):

$$R_{JET} \quad = \quad R_o \quad = \quad \int_0^\tau dt\, v_r \;\approx\; (c\tau)(R_G/2R_{JET})^{1/2} \;\approx\; 10^{-2}\,L \qquad (28)$$

where on the far right we solve $R_{JET}^{3/2} = c\tau(R_G/2R_{JET})^{1/2}$ using L from Eq. (8) and $(a\Omega/c\ \ln R/a) = 0.01$ from Eq. (12) and $\ln R/a = 20$. Eq. (28) agrees with our model values for R_o and L giving R_{JET} roughly consistent with observations [26].

Note that at first sight an accretion disk this large could not provide current carriers at large radii for the field solution of Figure 3 yielding field line lengths ≈ $L(B_\phi/B_z) >> ct$ at large r. Yet there is no other likely source, since the density in Eq. (1) is too low to ionize neutrals and inward diffusion of ambient ions is too weak [6]. The most likely resolution is analogous to the existence of closed 2D flux surfaces in laboratory spheromaks even when kinking 3D field lines remain connected to power from the gun [8,14]. Here also, the 2D solution of Figures 1 and 4 is probably due to kink instability producing 3D field lines of length < cτ, as in Fig. 5b [6].

Concerning electron synchrotron radiation from the jet, we first note that, while radiation from the runaway ion beam discussed in Section 3 is due to field line curvature, two-stream instability mentioned in Section 2 scatters electrons which then radiate due to Larmor radius curvature, giving the microwave and higher frequency radiation illuminating radiolobes [6]. Since in our model the power is concentrated in the central column, a natural explanation of synchrotron radiation from the radiolobes might be kink instability of the diffuse pinch as it creates a radiolobe, causing the pinch with its constricted central column to wander, loosely filling the radiolobe volume defined by the return current, as in the MHD simulation of Fig. 5b. That is, the apparent diffuse glow of a radiolobe would actually be produced by a glowing filament – the central column – which appears straight in 2D but loosely fills the radiolobe volume in 3D, with a number of turns of order $(c\tau/\pi L) \approx 30$ [6]. With sufficient resolution, this filamentary structure could be detected.

Since both ions and electrons are accelerated, the power in electron synchrotron radiation should be of order 1/2 $I\Delta V$ [6], where ΔV is the voltage drop along the central column that we estimated to be $\Delta V < V/\ \ln R/a_o = 0.05V$ by Eq. (15). Electron synchrotron wavelengths would be determined by the field B_o in the central column. For $B_o = 5\ x10^3$ gauss in Eq. (12), the predicted fundamental wavelength $\lambda_{SYN} = 10^4\ (\gamma_e/B_o)$ is in the cm range over the central column, as often observed, since γ_e is small due to radiative cooling [6]. This B_o corresponds to $M_{BH} \approx 10^8$ Suns. For other values of M_{BH}, $\lambda_{SYN} \propto B_o^{-1} \propto M_{BH}^{1/2}$ by the scaling of Section 2. The observed spectrum would include harmonics of the microwave fundamental and x-rays due to the high energy tail of the electron energy distribution.

We conclude with four additional comments on observables. First, the magnetic profiles derived in Appendix B imply synchrotron wavelengths increasing with r in the quasi-stable portion of the jet, perhaps accounting for observed illumination patterns with radial extent increasing with wavelength [27]. Secondly, synchrotron damping in the jet of magneto-rotational fluctuations propagated out of the disk may account for intense luminosity near the disk (see Appendix C). Thirdly, the spheromak-like magnetic field of Figure 1 is subject to rotationally-augmented "tilt" modes that could give rise to precessional motion accounting for rapid periodic changes in electromagnetic emission of

jets observed end-on, with polarization characteristic of synchrotron emission in the coherent magnetic field of the jet [28]. Precession rather than disruption might be expected for parameters close to marginal stability. For an isolated disk (no jet), the stability condition is $(\Omega/k_z v_A) \approx 0.2$ for the m = 1 tilt mode (with Alfven speed v_A) [29], similar to the stability criterion for the m = 0 magneto-rotational mode discussed in Appendix C. Finally, the asymmetric shape of some jet-radiolobe structures (as in Ref. [26]) can result from intergalactic "winds" pushing on the return current boundary, the jet inside always conforming to the boundary, as discussed in Appendix B [6].

6. Summary

We have arrived at a self-consistent accretion-driven magnetic structure producing UHE cosmic rays. In Appendices A, B, and C we show how accretion sustains a self-excited dynamo driving current that creates the observed jet/radiolobe structures that serve as the accelerator in Section 3, illustrated in Figure 1 and MHD simulations in Figure 5. In Section 2, we argue that dynamo torque dominates the accretion process, giving in Appendix A a magnetically-dominated modification of the viscosity-driven Standard Model of accretion [2, 30]. Macro-stability of the configuration is shown to arise from a tendency of the current to hover at just the value required to eject a jet.

The new feature of our cosmic ray model is quasi-steady acceleration of cosmic ray ions, mainly in the central column and its return current in Figure 1 that are insensitive to accretion details outside of the compact central column radius $a \approx 10R_G$. Achieving high energies in the UHE range requires a new mechanism, the DCLC velocity-space instability caused by runaway acceleration creating a non-Maxwellian ion beam, discussed in Section 3. The model also may explain the remarkable collimation of jets, discussed in Section 5.

The predicted disk radiation, in Appendix A, is similar to the Standard Model. Unique predictions concern the jet/radiolobe structure created by the dynamo. As with the Standard Model, we take the black hole mass M_{BH} and the accretion rate as input parameters. From these 2 inputs, the model makes 7 predictions roughly consistent with data: the length of the collimated jet in Section 2; the steady state cosmic ray energy spectrum, the maximum energy in this spectrum and the cosmic ray intensity reaching

Earth in Sections 3 and 4; and the jet radius, the synchrotron wavelength, and the synchrotron power in Section 5. The magnetic fields predicted by the model are also consistent with inferred field magnitudes in radiolobes, which account for the radiolobe radius at which magnetic pressure balances ambient pressure [16].

Based on these qualitative successes, we offer our model as a speculative but potentially self-consistent linkage of UHE cosmic rays to dynamo activity around black holes. Detailed verification of all features simultaneously requires new computer simulations and laboratory experiments. We have shown that it is essential to include in simulations kinetic instabilities needed to accelerate the cosmic ray ions. Understanding cosmic ray acceleration requires also collisionless experiments and kinetic simulations allowing ions to run away in the expanding nose in Fig. 1. Kinetic simulations at the level of sophistication currently available in plasma physics can calculate the cosmic ray spectrum estimated in Section 4. Kinetic transport coefficients introduced into 3D MHD simulations can provide a more accurate mapping of the evolving magnetic field.

Appendix A. Accretion-Driven Dynamo Model

In Appendices A, B and C, we attempt to justify the cosmic ray accelerator magnetic structure of the main text, illustrated in Figure 1, characterized by a dynamo-driven central column of current with a large inductance due to the surrounding diffuse pinch and radiolobe. To do so, we amend the accretion disk model of Shakura and Sunyaev [30], sometimes called the Standard Model, to include the effects of the dynamo magnetic field. Having developed a 0-D model for the dynamo driving the central column in Sections 2 and 3, as in the Standard Model the domain of interest here will be the extended dynamo driving the diffuse pinch, covering $a < r < R_o = R_{JET}$. As defined in Section 5, R_o is the dynamo O-point radius (where j_z and B_z change sign), growing for the lifetime of the system, Eq. (23). Like the edge of the rotor in Figure 2, R_o defines the boundary of power outflow from the dynamo. Though the jet current returns somewhere beyond $r > R_o$, this portion of the accretion disk where $\Omega(r)$ is small has little effect on the magnetics of the dynamo/jet, serving mainly as an accretion reservoir and electric potential reference point giving $V_{12} = \int_{R1}^{R2} dr\, r\Omega(r)B_z \approx \int_{R1}^{Ro} dr\, r\Omega(r)B_z$ as the voltage drop

between a current path leaving the dynamo at $r = R_1 < R_o$ and returning at $r = R_2 > R_o$ [6].

In developing our accretion model, we follow the discussion of the Standard Model in Ref. [2], Chapters 5 and 8, and its adaptation to AGN's in Appendix A of Ref. [17]. We begin with conservation laws for mass, momentum and heat, now adding Maxwell's equations and Ohm's Law:

$$\partial\rho/\partial t + \nabla\cdot\rho\mathbf{v} = 0 \qquad \text{(A1)}$$

$$\rho(\partial\mathbf{v}/\partial t) - c^{-1}\mathbf{j} \times \mathbf{B} = \mathbf{F} \equiv \mathbf{E}(\nabla\cdot\mathbf{E}/4\pi) - \rho(\nabla V_G + \mathbf{v}\cdot\nabla\mathbf{v}) - \nabla\cdot\underline{\mathbf{P}} \qquad \text{(A2)}$$

$$\partial(3nkT)/\partial t = P_{VISC} + c^{-1}\mathbf{j}\cdot\mathbf{E} - (P_{RAD}/H) \qquad \text{(A3)}$$

$$\partial\mathbf{B}/\partial t = -c\,\nabla \times \mathbf{E} \qquad \text{(A4)}$$

$$c^{-1}\partial\mathbf{E}/\partial t = \nabla \times \mathbf{B} - (4\pi/c)\mathbf{j} \qquad \text{(A5)}$$

$$\mathbf{E} + c^{-1}\mathbf{v} \times \mathbf{B} = 0 \qquad \text{(A6)}$$

where **E** is the electric field, **B** is the magnetic field with current density **j**, **v** is the fluid velocity, $\rho = nm_i$ is mass density, V_G is the gravitational potential, P_{RAD} is surface radiation power, and $\underline{\mathbf{P}}$ is the pressure tensor including radiation pressure P_{RAD}/c. In Eq. (A3), as in the Standard Model we neglect heat transport out of the disk but retain the viscous heating P_{VISC} of the Standard Model and surface radiation, H being the disk height. While we have omitted Spitzer resistivity η giving timescales $(4\pi H^2/\eta c^2) > \tau$, **E**, **B** and **v** will be understood to include both the mean fields and perturbations as needed, for example, a symmetrically averaged hyper-resistivity term $\langle \mathbf{v}_1 \times \mathbf{B}_1 \rangle$ in Ohm's Law, discussed in Section 3 [14]. Poisson's equation and $\nabla\cdot\mathbf{B} = 0$ must be satisfied at $t = 0$, preserved thereafter by $(\nabla\cdot)$ operating on Eqs. (A4,A5).

As in the Standard Model, we neglect collisional transport processes, so that hyper-resistivity and most especially the accretion velocity v_r arise only from turbulence

processes due to magneto-rotational instability (MRI), discussed in Appendix C. The neglect of collisions will be justified by the plasma density derived from the accretion disk model. That v_r plays the crucial role in creating a dynamo can be seen from Eq. (A4), which, together with Ohm's Law, yields the toroidal field equation $\partial B_\phi/\partial t = r\Omega\nabla\cdot\mathbf{B}_{POL}$ with poloidal **B**, now verified experimentally [3], and the poloidal field equation $\partial A_\phi/\partial t = (-v_r B_z + \langle v_{1z} B_{1r}\rangle)$ which requires v_r to sustain growth of the dynamo field B_z (while $\langle v_{1z} B_{1r}\rangle$ maintains quasi-steady state).

The electrostatic $\nabla\cdot\mathbf{E}$ in Eq. (A2) is important only in the sheath that dominates the ejection of ion current against gravity, giving Eq. (1) (see Ref. [6], Appendix A1). Otherwise, we can neglect $\nabla\cdot\mathbf{E}$ in **F**, even though the dynamo voltage is produced by electrostatic polarization charge. Comparing the electric force term $E_r(\nabla\cdot\mathbf{E}_r/4\pi)$ with $E_r = (v_\phi B_z/c)$ to the magnetic term $c^{-1}j_\phi B_z = \partial(B_z^2/8\pi)/\partial r$ gives at $r > a$ inside the dynamo the ratio $\approx 2(v_\phi/c)^2 \approx 0.1(a/r)$, hence small; and, projecting E_r into the jet, the ratio $(a\Omega/c)^2 < 0.04$ inside the central column, with $(a\Omega/c) = 0.2$ from Eq. (12), again a small effect.

We also construct from these equations the conservation of angular momentum, given by the z component of (**r** x) operating on Eq. (A2), and the conservation of energy, given by operating on Eq. (A4) by (**B**·), operating on Eq. (A2) by (**v**·) and adding the results to Eq. (A3) to obtain, with flux $\psi = \int_0^r 2\pi r dr\, B_z = 2\pi r A_\phi$ for vector potential A_ϕ:

$$\partial/\partial t\,(\rho r^2\Omega) \quad + \quad \nabla\cdot\rho\mathbf{v}\, r^2\Omega \quad - (\mathbf{r}x\nabla\cdot\underline{\mathbf{P}})_z \quad = \; c^{-1}r(j_z B_r - j_r B_z) \; = \; -c^{-1}\nabla\cdot\mathbf{j}(\psi/2\pi) \qquad (A7)$$

$$\partial/\partial t\,[(B^2/8\pi) + 3nkT + \rho\,(v^2/2)] + \nabla\cdot(c\mathbf{E}x\mathbf{B}/4\pi) \quad = \quad \mathbf{v}\cdot\mathbf{F} \; - \; (P_{RAD}/H) \qquad (A8)$$

Note that $\mathbf{j}\cdot\mathbf{E}$ (including hyper-resistivity) and also P_{VISC} only exchange energy, hence cancel out in Eq. (A8). Eq. (2) in Section 2 is the volume integral of Eq. (A8), giving the inductance from $(B^2/8\pi)$ and gravitational power from $\mathbf{v}\cdot\mathbf{F}$.

In Eq. (A7), on the far right we add to the torque $c^{-1}(\psi/2\pi)\nabla\cdot\mathbf{j} = 0$, giving $c^{-1}\nabla\cdot\mathbf{j}\psi$ which represents the conversion of rotational angular momentum into magnetic canonical angular momentum. Integrating Eq. (A7) over the surface of the disk gives, from $\nabla\cdot\rho\mathbf{v}r^2\Omega$, the radial accretion of angular momentum, and, from $\nabla\cdot\mathbf{j}\psi$, the axial ejection of

angular momentum into the jet, $\int d\mathbf{S}\cdot\mathbf{j}_z\psi$. In the absence of dissipation, $\nabla\cdot\mathbf{j}\psi$ would conserve angular momentum, finally recycling all of it where current returns to the disk somewhere beyond $r > R_{JET}$. In the outer portion of the return path carrying the central column return current, where DCLC instability satisfying Eq. (19) ejects cosmic ray ions, acceleration converts $\mathbf{j}\psi$ into kinetic angular momentum whereby each escaping ion carries with it a diamagnetic angular momentum arising from $j_\phi = nev_\phi \propto (-\nabla_z p/B^2)B_r$ with pressure p giving $m\gamma r v_\phi \propto (r_L\nabla_z\beta)e\psi \rightarrow e\psi$ in the nose, giving also $d\psi/dt = -(n^{-1}\nabla_z\cdot D\nabla_z n)\psi$ which kills ψ, leaving $\nabla\cdot\mathbf{j} = 0$ (not flux surfaces) as the proper description of the return current channel. The DCLC instability criterion, Eq. (19), cannot be satisfied over the large dimension of the diffuse pinch, so that deep inside the diffuse pinch angular momentum may continue to be recycled. Since most of the angular momentum is extracted far out in the diffuse pinch, it follows that most of the angular momentum, but little of the energy, may be recycled to the outer region of the disk, beyond the active dynamo.

As in the Standard Model, we will apply the Thin Disk approximation in order to reduce 2D Eqs. (A1)-(A8) to 1D, by averaging over the disk height [2]. We first recover the main results of the steady state Standard Model by dropping all time derivatives and integrating Eqs. (A1), (A7) and the z-component of Eq. (A2) over the disk height H, giving, with $\Sigma = \rho H$ and $M^* \equiv dM_{BH}/dt$:

$$M^* = -2\pi\Sigma r v_r \qquad \text{(A9)}$$

$$(IB_z/c) = -M^* r^{-1}\partial/\partial r\, r^2\Omega[1 - \nu(v_r\Omega)^{-1}\partial\Omega/\partial r] \qquad \text{(A10)}$$

$$1/2\,\Sigma H(M_{BH}G/r^3) = P \equiv 2n_i kT + c^{-1}P_{RAD} + P_z, \quad P_z = \alpha_z(M^*\Omega/2\pi r)(H/r) \qquad \text{(A11)}$$

In Eq. (A9), we neglect mass ejected into jets by assuming $v_z = 0$ in Eq. (A1), whereby integrating Eq. (A1) over $2\pi r dz$ and dropping $\partial M^*/\partial t$ gives $r^{-1}\partial M^*/\partial r = 0$ with $M^* = 2\pi\int_0^H dz\rho v_r = 2\pi\Sigma r v_r$, hence the constant accretion rate in Eq. (A9). In Eq. (A10) obtained from Eq. (A7), ν is the viscosity coming from $\nabla\cdot\underline{\mathbf{P}}$ [2] and we anticipate the discussion in Appendix B justifying $B_r \approx 0$ inside the dynamo (except near the midplane for the

quadrupole field of Refs. [17, 18]). Then we can drop B_r in the torque $r(j_z B_r - j_r B_z)$, giving on the left hand side of Eq. (A10) $\int_0^H 2\pi r dz(-c^{-1} j_r B_z) = -(I_r B_z/c) = (I B_z/c)$ where $I_r(r)$ is the downward-flowing dynamo current j_r integrated across the disk, and $I_r = -I$, shown by integrating $\nabla \cdot \mathbf{j} = 0$ (obtained from the divergence of Eq. (A5) with $\partial \mathbf{E}/\partial t = 0$) giving $\int_0^H 2\pi r dz[r^{-1} \partial/\partial r(r j_r) + \partial/\partial z\, j_z] = \partial/\partial r\,(I_r + I_z) = 0$ giving $-I_r = I_z \equiv I = \int_0^r 2\pi r dr j_z$. Eq. (A11) is the integral across the disk height of the z-component of Eq. (A2). On the left hand side, we drop $(\mathbf{v} \cdot \nabla \mathbf{v})_z$ and take $(\nabla V_G)_z \approx (M_{BH} G z/r^3)$ with black hole mass M_{BH} and Newtonian gravitational constant G [2]. On the right hand side $n_i = (\Sigma/m_i H)$, $c^{-1} P_{RAD}$ is radiation pressure and P_z is axial pressure due to magneto-rotational (MRI) turbulence, derived in Appendix C. Another condition is obtained by integrating Eq. (A3) over the disk height, giving [2]:

$$P_{HEAT} \equiv H[P_{VISC} + P_H] = P_{RAD} \quad , \qquad P_{HEAT} = v_r H\, \partial/\partial r\, (B_z^2/8\pi) \qquad \text{(A12)}$$

where P_{HEAT} is MRI heating derived in Appendix C.

For the Standard Model, taking M_{BH} and M^* as known and dropping magnetic terms and our MRI turbulence-derived terms leaves 4 equations, Eqs (A9) – (A12), with 4 unknowns, v_r, H, Σ and T, if we guess Ω (say, Keplerian). Then angular momentum is conserved only if, following Shakura and Sunyaev, one postulates a viscosity ν large enough to satisfy $[1 - \nu(v_r \Omega)^{-1} \partial\Omega/\partial r] = 0$ in Eq. (A10). This approach is used to obtain concrete parameters in discussing the stellar-collisional magnetic pumping method of helicity ejection to create a self-excited dynamo, in Ref. [17], it being assumed that the growth of the dynamo field will not much perturb the accretion process.

In Appendix C, we will find that the disk parameters obtained in Ref. [17] would be unstable to magneto-rotational instability (MRI), a currently-favored alternative means of conserving angular momentum [2, 31]. Another candidate – Rossby vortex instability – may be important in the accretion reservoir of Figure 1 [5] but this instability may be suppressed by the strong magnetic fields in the dynamo [32]. Here we will show, in Appendix C, that MRI transport sustaining magnetic jets can fully account for angular momentum conservation, thus prompting us to take $\nu = 0$, which also turns out to simplify the model considerably.

In the remainder of this Appendix, we will complete the set of equations required for our model, 7 in all, including the 4 above for the Standard Model, but retaining the magnetic terms and setting $\nu = 0$. Our 7 equations yield seven variables, the Standard model set v_r, H, Σ and T together with I, B_ϕ and also Ω, which is determined by the model. As in the Standard Model, physical plausibility rests on explaining the accretion velocity v_r, in our case by magneto-rotational turbulence shown to be the surviving MHD instability in Appendix B. A complete justification for setting $\nu = 0$ would require showing also that non-magnetic modes are either stable or contribute negligible transport, true for the Standard Model $\nu = c_S/H$ as noted in Section 2.

Our three additional equations are energy conservation, Eq. (A8); the radial force balance, obtained from the r component of Eq. (A2); and a new closure to replace the assumed viscosity of the Standard Model. The useful form of energy conservation is obtained by integrating Eq. (A8) over the disk height, now retaining $\mathbf{v}\cdot\mathbf{F}$ and Ohm's Law in the Poynting vector to obtain:

$$\{\Omega(IB_z/2\pi c) + Hr\Omega F_\phi\} - P_{RAD} = - Hv_rF_r \qquad (A13)$$

$$F_\phi = - \rho[v_r\partial(r\Omega)/\partial r + \Omega v_r] = (M^*/2\pi H)[\partial(r\Omega)/\partial r + \Omega] \qquad (A14)$$

$$\{\Omega(IB_z/2\pi c) + Hr\Omega F_\phi\} = - (\Omega M^*/2\pi)[r^{-1}\partial(r^2\Omega)/\partial r - \partial(r\Omega)/\partial r - \Omega] = 0 \qquad (A15)$$

where on the left hand side of Eq. (A13) the Poynting vector term gives $\int dz(r\Omega B_z B_\phi/4\pi) = (r\Omega B_z/4\pi)(2I/cr) = \Omega(IB_z/c)$, showing that the jet power is just Ω times its angular momentum ejection rate, Eq. (A10). For any quasi-steady rotation profile $\Omega(r)$, Eq. (A15) gives exact cancellation of the Poynting term with $Hr\Omega F_\phi$, confirming that it is $r\Omega F_\phi$ that performs the work extracting the stored rotational energy that is ejected by the non-radiative contribution to the Poynting vector. Substituting Eq. (A15) into Eq. (A13) gives:

$$F_r = - \rho[(M_{BH}G/r^2) - r\Omega^2 + \partial/\partial r\,(v_r^2/2)] - \partial P/\partial r = (Hv_r)^{-1}P_{RAD} \qquad (A16)$$

We will find that P_{RAD} is negligible compared to terms in F_r, giving $F_r \approx 0$. Introducing $F_r = 0$ into the radial component of steady-state form of Eq. (A2) gives:

$$- c^{-1}(j_\phi B_z - j_z B_\phi) = (1/8\pi)[\partial/\partial r\, B_z^2 + r^{-2}\, \partial/\partial r\, (2I/c)^2] = F_r = 0 \qquad (A17)$$

This key result, coming from dropping both $\nabla\cdot\underline{\mathbf{P}}$ ($\nu = 0$) and B_r in Eq. (A7), is quite robust, the omitted torque $\propto j_z B_r$ giving $(j_z B_r/j_r B_z) = (HI^{-1}\partial I/\partial r)(B_r/B_z) = (a/r)^{1/2}(B_r/B_z) << 1$ for any likely corrections for finite B_r. Eq. (A17) is the principal simplification of our Thin Disk model, giving however only the z-averaged B_z etc. inside the dynamo, while the actual B_ϕ satisfies $\partial B_\phi/\partial z = - (4\pi/c) j_r$. Otherwise, approximations giving Eq. (A17) will be found to follow if we set $B_r = v_z = \partial/\partial z(v_\phi B_z) = \partial/\partial r(r\rho v_r) = 0$. The field solution obtained from Eq. (A17), in Appendix B, is the exact solution for the jet where, except at the nose, we can take $B_r = 0$ exactly, a manifestation of pinch forces causing collimation of the jet. In this way our dynamo solution provides the correct field from which the jet/radiolobe inductance was calculated in Section 2.

Finally, as closure, we use the fact that unstable plasmas typically achieve steady state by hovering near the marginal condition for instability, giving for the magneto-rotational mode:

$$(\pi/H)^2(B_z^2/4\pi\rho) = (\pi/4)(B_z^2/\Sigma H) = - r\partial/\partial r\, \Omega^2 \qquad (A18)$$

with wavenumber $k_z = (\pi/H)$. Instability occurs if the left side is smaller than the right hand side [31].

The seven Eqs. (A9) - (A12) and Eqs. (A16) – (A18) with $\nu = 0$ form a complete set to describe a steady state accretion disk at the margin of magneto-rotational instability. We rewrite these model equations as:

$$[\Omega_{KEP}^2 - \Omega^2 + r^{-1}\, 1/2\, \partial/\partial r\, v_r^2] = 0 \qquad \text{from Eqs. (A16)} \qquad (A19a)$$

$$v_r = - 1/2\, r(\Omega_{KEP}^2/\alpha_z\Omega) \qquad \text{from Eqs. (A9,A11)} \qquad (A19b)$$

$$\Sigma = -(M^*/2\pi r v_r) \quad \text{from Eqs. (A9)} \qquad (A19c)$$

$$(IB_z/c) = -M^* r^{-1}\partial/\partial r\,(r^2\Omega) \quad \text{from Eq (A10)} \qquad (A19d)$$

$$\Sigma H = (\pi/4)[B_z^2/(-r\partial\Omega^2/\partial r)] \quad \text{from Eq. (A18)} \qquad (A19e)$$

$$P_{HEAT} \equiv Hv_r\,\partial/\partial r\,(B_z^2/8\pi) = (\sigma T^4/\tau_{OP}) \quad \text{from Eq. (A12)} \qquad (A19f)$$

$$\partial/\partial r\, B_z^2 + (1/r^2)\,\partial/\partial r\,(2I/c)^2 = 0 \quad \text{from Eqs. (A17)} \qquad (A19g)$$

where $\Omega_{KEP}^2 = M_{BH}G/r^3$ is Keplerian rotation, $\sigma = 5.7 \times 10^{-5}$ in cgs units is the Stefan-Boltzmann coefficient, and $\tau_{OP} = 1 + \Sigma\kappa_R$ with Thomson opacity $\kappa_R = 0.4$ [17]. Eq. (A19c) is just mass conservation, Eq. (A9). As justified below, we drop radiation and thermal pressure in the axial force balance, Eq. (A11), whereby using Eq. (A9) to eliminate M* in Eq. (A11) gives v_r in Eq. (A19b).

Eqs. (A19) have been organized to facilitate finding asymptotic solutions of greatest interest. The radial force balance Eq. (A19a), together with $v_r \propto \Omega^{-1}$ in Eq. (A19b), suggests Keplerian scaling for Ω. In fact, for any asymptotic power law $\Omega^2 \propto r^{-K}$, solutions of Eq. (A19a) exist only if K = 6 – K = 3 giving Keplerian K = 3. Letting $\Omega^2 = C/r^3 = X\Omega_{KEP}^2$, Eq. (A19a) becomes a quadratic equation with solutions:

$$X = 1/2\,[1 +/- \sqrt{[1 - (1/2\alpha_z^2)]} \qquad (A20)$$

Real solutions exist only if the MRI axial pressure parameter $\alpha_z^2 > 1/2$, or $k_zH < \sqrt{2}(-\omega/\Omega) < \sqrt{2}$, $-\Omega$ being the maximum MRI growth rate [31]. This violates our nominal boundary condition $k_zH > \pi$. However, given the strong tendency toward quasi-steady state by the arguments in Section 2 and Appendix B below, we interpret this result as another indication of marginal stability by taking $\alpha_z^2 = 1/2$. Then X = 1/2, giving $\Omega = -(1/\sqrt{2})\Omega_{KEP}$ and $v_r = 1/2\; r(\Omega_{KEP}^2/\Omega\alpha_z) = -r\Omega_{KEP}$. From Eqs. (A10,A13), the corresponding Poynting vector power $(-r\Omega B_z B_\phi/4\pi) = \Omega M^*(r^{-1}\partial(r^2\Omega)/\partial r = 1/8\; M^*\Omega_{KEP}^2$

which is 25% of the gravitational power, hence an efficiency f = 25% in converting gravitational power to jet power, the remainder being convected inward toward the black hole (as v_r and $r\Omega$ kinetic energy). We also used f = 25% for the Central Column in Section 2

Substituting $v_r = - r\Omega_{KEP}$ into Eq. (A19c) gives Σ. The remaining asymptotic parameters can be found from an expectation, verified in Appendix B, that I should approach a constant value at large r. Then $B_\phi = (2I/cr) \propto 1/r$ and, by Eq. (A19d), $B_z \propto \Omega \propto \Omega_{KEP} \propto 1/r^{3/2}$ as anticipated in Eq. (5), giving the inductance in Eq. (6). With $B_z = B_\phi = B_a$ at r = a, we can write $B_z = B_a(a/r)^{3/2}$ and $I = (caB_o/2)$, whereby Eq. (A19d) yields a value for B_a and Eq. (A19e, A19f) yield H and T, while Eq. (A19g) only gives details of I(r) near r = a, in Appendix B. For $M_{BH} = 10^8 M_{SUN}$ and $\tau = 10^8$ yrs giving $M^* = (M_{SUN}/\tau)$ yielding the central column parameters in Eq. (12), we obtain:

$$\Omega = - 0.7\ \Omega_{KEP} \qquad \text{(A21a)}$$

$$v_r = - r\Omega_{KEP} \qquad \text{(A21b)}$$

$$\Sigma = 5\ (a/r)^{1/2} \qquad \text{(A21c)}$$

$$H = 0.7\ a\ (r/a)^{1/2} \qquad \text{(A21d)}$$

$$T = 6 \times 10^4\ (a/r)^{1/2} \qquad \text{(A21e)}$$

We expect $B_a < B_o$ due to additional toroidal current inside the central column. The ratio B_o/B_a is related to our estimate a/R_G,= 10 in deriving numbers in Eq. (12), Section 2. The derivation in Section 2 gives $IV = 1/2\ (a\Omega_{KEP})(aB_0)^2 = f[1/2\ M^*c^2]$ while the derivation from Eq. (A19d) yields $(IB_z/c) = ½\ aB_a^2 = -1/2\ M^*\Omega = 1/2\ (0.7)M^*\Omega_{KEP}$, all quantities evaluated at r = a. Eliminating the radius a gives:

$$(a\Omega_{KEP}/c)^2 = (R_G/2a) = (f/0.7)(B_a/B_0)^2 \approx 0.09f \qquad \text{(A22)}$$

Then a/R_G is determined by choosing a reasonable B_a/B_0 matching the Keplerian zone and the central column at r = a in Figure 3. The numbers above correspond to $B_a/B_0 = 1/4$. For f = 0.25 above, this gives $a \approx (5/f)R_G = 20R_G$ rounded to $a = 10R_G$ in Section 2.

The line density Σ in Eq. (A21c) is about 10^4 times smaller than that for the Standard Model in Ref. [17], while, assuming black body radiation, the surface temperatures are comparable due to a large τ_{OP} for the Standard Model ($\tau_{OP} \approx 1$ for our model). Since we neglect radiation, of greater importance is the MRI-derived power driving radiation in Eq. (A19f), of order $\Omega(B_z^2/8\pi) \propto \Omega/r^3$ while the jet Poynting power is asymptotically larger, of order $\Omega(B_\varphi B_z/8\pi) \propto \Omega/r^{5/2}$. Radiation pressure and thermal pressure are also small, as assumed. Dropping $\partial P/\partial r$ in Eq. (A16) is similarly justified by $P \approx P_z \propto (\Omega H/r^2) \propto (1/r)^{3/2}(1/r)^{1/2}(1/r) = 1/r^3$, giving $\partial P/\partial r \propto (1/r^4)$ while all other terms are $\propto (1/r^3)$.

Radiation is not negligible at $r < a$, the fraction radiated determining τ by Eq. (23). Near $r = a$, the ratio of surface heating power $\Omega H(3B_o^2/8\pi)$ (from Eq (A19f)) to the Poynting power is:

$$\text{(Heating/Jet Power)} = [\Omega H(3B_o^2/8\pi)]/[\Omega(aB_o^2)/4\pi] = 3/2\ (H/a) \approx 1 \qquad \text{(A23)}$$

where, at $r = a$, $H/a = 0.7$ by Eq. (A21). Thus inside the central column, heating converted to radiation is comparable to the jet power, so that radiation is also about 25% of the gravitational power entering the central column, as we assumed in deriving τ in Eq. (23).

Note that, though v_r derived in Appendix C exists only by virtue of MRI instability, the results of Eq. (A21) do not depend explicitly on perturbation amplitudes, subsumed here in v_r (or M*), as discussed in Appendix C.

Note also that integrating $\Sigma(r)$ in Eq. (A21c) over the disk of radius R_{JET} in Eq. (28) gives a mass that already equals M_{BH} at $r = 0.2\ R_{JET}$. This violates our model assumption that M_{BH} dominates gravitational attraction, requiring some adjustment of the model near the dynamo O-point at $r = R_{JET}$.

Otherwise, Eqs. (A9) - (A12) and (A16) – (A18) constitute a complete model, including a calculation of $\Omega(r)$, down to $r \approx$ a few R_G where internal kink modes and finally general relativity must be taken in account. Even without these complications, as shown in Appendix B our asymptotic results giving Keplerian rotation finally fail, at a radius that we will identify with $r = a$, the radius of the central column in Figure 1.

Appendix B. Magnetic Profiles, Inductance

In this Appendix, we calculate magnetic profiles at r > a, still resorting to the 0-D model of Section 2 to describe the central column, at r < a. We begin by applying Eq. (A19g) and Eq. (A10) with $\nu = 0$ to derive the field inside the disk, rewritten as:

$$\partial(B_z^2)/\partial r + r^{-2}\,\partial(rB_\phi)^2/\partial r \;=\; \partial(B_z^2)/\partial r + r^{-2}\,\partial(g/B_z^2)/\partial r \;=\; 0 \qquad \text{(B1)}$$

$$g(r) \;=\; [2(M^* r^{-1}\partial/\partial r\, r^2\Omega)]^2 \qquad \text{(B2)}$$

Changing variables to dimensionless quantities $F = (B_Z^4 r^2/g)$ and $x = (r/R_1)$ gives:

$$dF/dx \;=\; [F/x(F-1)][(K+2)F + (K-2)] \qquad \text{(B3)}$$

where $K = (-\,d\ln g/d\ln x) = 3$ for Keplerian rotation. Further transforming to variables lnF and ln x yields, for $\Omega^2 \propto x^{-K}$ with any constant K, an integrable form with solution:

$$x \;=\; F^{-k}\,[(K+2)F \;+\; (K-2)]^p \qquad \text{(B4)}$$

where $k = (1/(K-2))$, and $p = [2K/(K^2-4)]$. Plotting F versus x discloses two branches, the lower one being the physical solution for an isolated disk producing its own magnetic field (a "spheromak", while the upper branch requires an external toroidal field, giving a "tokamak" or "reversed-field pinch"). The physical solution lies to the right of a value x_o found by differentiating Eq. (B4) by d/dF. This gives $dx/dF \propto (F-1)$, hence a turning point where F = 1.

The lower physical branch is plotted in Figure 3 for Keplerian K = 3. Physically, $r_o = 8.6\ R_1$ is the radius inside which Keplerian rotation is no longer possible, not determined here since the scaling number R_1 is not determined. We will identify $r_o = a$, the radius of the central column carrying most of the current, taken as $a = 10\ R_G$ in Section 2. As justification, we note that, at $r = r_o$, I is a fraction 1/1.7 = 60% of its asymptotic value, indicating that current continues to flow radially downward through the

dynamo and out through the central column. Angular momentum can continue to be extracted at r < a, as is required to eject power, but not at the Keplerian rate.

As noted in Section 2, the Thin Disk magnetic profiles in Figure 3, describing a dynamo, match perfectly onto a force free jet, also described by Eq. (B1). With this interpretation, the fact that I is concentrated in the central column, giving $B \approx B_\phi = (2I/cr)$ for r > a in Figure 3, justifies the inductance in Eq. (6) giving slow expansion of the jet in Eq. (7), giving then the cosmic ray accelerator electric field, Eq. (9), if also the nose maintains its shape during expansion of the jet (constant v_z at the nose, giving $E_r = (v_z B_\phi/c) \propto r^{-1}$). That the blunt nose of Figure 1 should persist is due to jet dynamics, as follows.

Jet dynamics including the nose is described by Eqs. (A2) - (A4). For slow expansion, dynamics can be approximated as a succession of force-free equilibria satisfying:

$$\lambda \mathbf{B} \quad = \quad (4\pi \mathbf{j}/c) \quad = \quad \nabla \times \mathbf{B} \qquad \text{(B5)}$$

where λ must match the corresponding quantity at the surface of the dynamo. Unbounded solutions yield "pre-bubbleburst" current levels concentrated near the black hole (I < that in Eq. 4), as in the spherical self-similar solutions of Refs. [33,34]. Higher currents yield the cylindrical jet solution of Figure 1 inside the return current boundary, uniquely determined by introducing into Eq. (B5) the λ(ψ) for the disk magnetic field [35] (asymptotically $\lambda \propto r^{-3/2} \propto \psi^{-3}$ for the field in Fig. 3, where $\psi = \int_0^r 2\pi r dr B_z$). Mapping λ(ψ) by Eq. (B5) is equivalent to "winding out flux" as in Ref. [15], except that plasma dynamics plays a key role in determining the evolving boundary shape. Figure 4 plots flux surfaces $\psi = \int_0^r 2\pi r dr B_z(r)$ for an equilibrium similar to Figure 3. Note that straight flux surfaces launched with $B_r = 0$ at the disk remain straight up the nose.

For typical laboratory spheromaks (and MHD simulations), field dynamics is determined by the Alfven speed. For the density of Eq. (1), $v_A \rightarrow c >> d\langle L\rangle/dt$ so that inside the boundary a small net **j** x **B** force (together with electromagnetic wave propagation into vacuum regions) continuously adjusts **B** as needed to maintain approximately the equilibrium solution of (B5) inside the return current boundary.

Evolution of the boundary is determined by its interface with ambient pressure p_{AMB} pushed ahead by the advancing nose, described approximately by:

$$nm_i\, d(\gamma \mathbf{v}_\perp)/dt = c^{-1}\mathbf{j}x\mathbf{B} - \nabla p_{AMB} \quad \text{(B6)}$$

$$d(B^2/8\pi)/dt = - \mathbf{v}_\perp \cdot \nabla p_{AMB} \quad \text{(B7)}$$

Eq. (B6) is an approximate version of Eq. (A2) including a relativistic Lorentz factor γ introduced inside the convective derivative d/dt. We ignore gravity; also shocks in the ambient gas, found unimportant in Ref. [10], as expected for an inductively-limited dL/dt. For a thin return layer, we can approximate $c^{-1}\mathbf{j} \times \mathbf{B} \approx - \nabla(B^2/8\pi)$ giving the "hoop force" characteristic of confined poloidal current loops. In metal coils, the hoop force is taken up by material forces inside the coils. Here the hoop force matches inertia and/or ambient pressure. Inside the return current channel where the pressure is small, $\nabla(B^2/8\pi) \approx 0$ whereby $B_\phi = (2I/cr)$ falls to zero and B_{POL} increases, finally giving $B_{POL} = (2I/cr)$ at the junction with the pressure wall. This B_{POL} induces j_ϕ inside the pressure wall, thereby transferring the hoop force as $- \nabla(B_{POL}^2/8\pi)$. Thus, inside the pressure wall:

$$nm_i\, d(\gamma \mathbf{v}_\perp)/dt = - \nabla[(B_{POL}^2/8\pi) + p_{AMB}] \quad \text{(B8)}$$

with boundary condition $B_{POL} = (2I/cr)$ at the junction with the return current.

In Figure 1, the radial boundary r = R occurs where the right hand side of Eq. (B8) becomes zero [10, 15, 16], while hoop forces overwhelming pressure at the nose tend to stretch the nose into the blunt shape of Figure 1. This occurs if, wherever the nose might be temporarily indented, $(\mathbf{v}_\perp)_r >> \langle dL/dt \rangle$, the average axial speed of the advancing nose. For numbers in Eq. (12), no matter what the shape of the nose, $\langle dL/dt \rangle << c$ while, like Eq. (11), Eq. (B8) yields $v_\perp = v_A$, now determined by the ambient pressure. The pressure balance at r = R determines p_{AMB} in terms of I (actual ion pressure or effective pressure if collisions couple ions and neutrals), giving at smaller radii $v_A = (v_0\sqrt{(R/r)/\gamma})$ $\rightarrow c$ with typical ambient thermal speed $v_o \approx 10^8$ cm/sec (Kev) [5]. Then over most of

the nose $v_\perp = v_A >> <dL/dt>$, giving time for hoop forces to straighten the nose, as in the simulation of Figure 5a. As expected, artificially modifying the flux-generator "gun" to enhance $v_z >> v_r$ near the axis yielded a focused jet of small radius on axis.

This fluid description must be tested against particle dynamics, giving "drift" motions in the non-uniform magnetic field of the nose that would cause ions to escape axially. Drift speeds $\approx v_\perp(r_L/r)$ add a hot ion loss nominally comparable to DCLC loss, but only DCLC also recycles ambient cold ions inward as we found to be essential in Section 4.

Taken together Eqs. (B7,B8) are the 2D equivalent of 1D Eqs. (2,11) which we found to give a stable jet at constant current I in Eq. (4), due to competition of dI/dt and $d\Lambda/dt$ in constant $V = Id\Lambda/dt + 2(dI/dt)\Lambda$ in Eq. (7) with variable inductance $d\Lambda/dt \propto dL/dt$ and $dL/dt \rightarrow v_A$ for free expansion in Eq. (11). Integrating Eq. (B7) over the volume bounded by the return current gives an equation analogous to Eq. (7), now with inductance $\Lambda = (2\int d\mathbf{x}B^2/8\pi I^2) \propto$ an average value <L> responsive to the shape of the nose. In Appendix C, we will find that the fluctuation levels required to sustain the quasi-steady state are comparable to the mean field, giving a "noisy" system. Nonetheless, the powerful tendency to maintain current flow in an inductively-dominated circuit should maintain on average the quasi-steady state current in Eq. (4).

Though not important for inductance, details of the diffuse pinch equilibrium in Figure 1 are important for our discussion of jet collimation and stability in Section 5. Solutions of Eq. (B5) always yield a collimated jet with a radius determined by pinch forces, and a return current conforming to the boundary [35]. As with laboratory guns, this jet must be matched to the dynamo "gun" whose properties are determined by angular momentum ejection, giving the solution of Figure 3. However, for $B_r = 0$, the disk solution of Figure 3 is also a solution in the jet (out to the nose), giving a perfect match. At large r, at any time t this solution has field line lengths $t(dL/dt)(B_\varphi/B_z) = 0.01ct(r/a)^{1/2} > ct$ for $r/a > 10^4$ so that at large r the disk would not be accessible as a source of ions. Yet ion current carriers in the diffuse pinch must come from the disk, since the density in Eq. (1) is too low to ionize ambient neutrals penetrating the jet/radiolobe structure, and inward diffusion of ions from the ambient pressure wall (for example, by DCLC instability in Eq. (19)) cannot penetrate to large distances. Yet the

persistence of MRI accretion driving the dynamo to $r \approx R_{JET} \approx 10^8$ a in Appendix C, and the robustness of arguments giving Figure 3 as the unique field solution accounting for angular momentum conservation during accretion, argue strongly for this solution. The most likely resolution, analogous to the existence of closed 2D flux surfaces in laboratory spheromaks even when 3D field lines maintain contact to the gun [8,14], is kink instability producing 3D field lines of length $< c\tau$, also the explanation of the 3D simulation, Figure 5b, versus the 2D structure in Figure 5a.

The most likely instabilities facilitating connection of the diffuse pinch to the disk are the external kink modes discussed in Section 5. The internal kink modes tend to be stable. To see this, we apply the following approximate stability criterion [36,37]:

$$(L/2\pi)q^2|\lambda'/q'| < \quad 1 \quad \text{stable, internal kink} \qquad \text{(B9)}$$

where $\lambda = (4\pi j_z/cB_z)$ and $q = (2\pi rB_z/LB_\phi)$, and $(n - m/q) \approx q'/q^2$ with $q' = dq/dr$ approximates the resonance at $q = m/n$ for azimuthal mode number m and axial mode number n [36]. For $r > a$, integrating Eq. (A17) with $B_z = B_o(a/r)^{3/2}$ gives $I(r) = 1.7I\sqrt{(1-0.75a/r)}$, hence $j_z = (I(r)'/2\pi r) = (Ia/3\pi r^3)$ and $\lambda = (4/3a)(a/r)^{3/2}$. Substituting this into Eq. (B9), along with $q = (2\pi r/L)(a/r)^{1/2}$ with $B_\phi = B_o(r/a)$, we obtain stability if $r/a > 4$ which is satisfied over most of $r > a$ in the diffuse pinch. Internal modes can be unstable in the central column ($r < a$) and probably drive $E_{||} \propto \delta B^2$ in Eq. (13). Since L cancels in Eq. (B9), internal modes can have short axial wavelength, allowing growth to saturate over a short distance whereas the external modes discussed in Section 5 grow exponentially over L, yielding δB too weak to drive $E_{||}$ over most of the jet length.

We conclude this section with an additional comment on how $B_r = 0$ in the field solution of Figure 3 persists in Figure 4. Figure 4 was calculated by the Corsica code [35], which solves the Grad-Shafranov equation for zero pressure, equivalent to Eq. (B5), given by:

$$r\partial/\partial r(r^{-1}\partial\psi/\partial r) + \partial^2\psi/\partial z^2 = -[(rB_\phi)\partial(rB_\phi)/\partial r](\partial\psi/\partial r)^{-1} = -\lambda\int_0^\psi d\psi\,\lambda \qquad \text{(B10)}$$

where $\psi = rA_\phi$ (dropping 2π). On the far right we use $rB_\phi = \int_0^r r\,dr\,(4\pi j_z/c) = \int_0^r r\,dr\,\lambda B_z = \int_0^\psi d\psi\,\lambda$. Setting $B_r \propto \partial\psi/\partial z = 0$ and multiplying Eq. (B10) by $(B_z/r) = r^{-2}(\partial\psi/\partial r)$ gives exactly Eq. (A19g) giving Eq. (B1) that we solved to obtain Figure 3. In Corsica, $\psi(r,0)$ at $z = 0$ is a boundary condition, and the functional form $\lambda(\psi)$ must be prescribed. Requiring $\lambda(\psi)$ to match Figure 3 at $z = 0$ means that $\lambda(\psi)$ satisfies Eq. (B10) at $z = 0$ with $\partial\psi/\partial z = 0$, which remains the soltuion up to the nose.

Appendix C. MRI-Driven Accretion

In this Appendix, we show that the Standard Model as applied to AGN's in Ref. [17] would be unstable, which motivated our alternative model developed in Appendix A based on the magneto-rotational instability (MRI), supplementing the stellar collision mechanism of Ref. [17]. We then derive MRI accretion rates and other processes needed for the model.

We begin by establishing the ordering for the **v** x **B** term in Ohm's Law, Eq. (A6). Even at the modest temperatures of Eq. (A21e), or the Standard Model [17], Spitzer resistivity η would give Ohmic decay times $(c^2\eta/a^2) >> \tau$, giving then $\eta\mathbf{j} << c^{-1}(\mathbf{v} \times \mathbf{B})$ and an Ohm's Law in which only turbulence provides dissipation of the mean fields **E** and **B**. Dropping Spitzer resistivity, we apply an ordering in which the unperturbed $v_r = v_z = B_r = E_\phi = E_z = 0$ and $(1/k_z r) \propto H/r$ and $\partial/\partial r$ are small, consistent with our thin disk solution, Eqs. (A19), giving:

$$\underline{\mathbf{r}}\,(E_r + c^{-1} v_\phi B_z) + c^{-1}\,[-\underline{\boldsymbol{\phi}} <v_{2r}> B_z + <\mathbf{v}_1 \times \mathbf{B}_1>] = 0 \qquad (C1)$$

with unit vectors $\underline{\mathbf{r}}$ and $\underline{\boldsymbol{\phi}}$. For simplicity, we will apply quasi-linear theory to estimate perturbations $\mathbf{v}_1$ and $\mathbf{B}_1$. Note that the accretion velocity $v_r \equiv <v_{2r}>$ is a transport quantity, reflecting the fact that accretion requires transport across the dynamo magnetic field.

Eq. (B9) showing that internal kink modes with azimuthal mode numbers $m \geq 1$ are stable at $r > 9/4$ in the diffuse pinch applies also in the disk having the same field profiles. Then the $m = 0$ MRI mode is likely to be the dominant instability, most simply analyzed omitting B_ϕ and taking B_z to be locally uniform in WKB approximation, with

wavenumber k_z along z and both $\mathbf{v}_1$ and $\mathbf{B}_1$ perpendicular to the z axis. Solving the linearized Faraday's Law for $\mathbf{v}_1$, for perturbations $\propto \exp(-i\omega t + ik_z z)$, gives:

$$v_{1r} = -(\omega/k_z)(B_{1r}/B_z) \quad \text{(C2)}$$

$$v_{1\phi} = -(\omega/k_z)(B_{1\phi}/B_z) \quad \text{(C3)}$$

Combining Eqs. (C2) – (C3) with the linearized momentum equations including rotation gives the MRI dispersion relation [31]:

$$\omega^4 - \omega^2[\kappa^2 + 2k^2 v_{Az}^2] + k^2 v_{Az}^2\{k^2 v_{Az}^2 + r\,\partial\Omega^2/\partial r\} = 0 \quad \text{(C4)}$$

where $\kappa = \sqrt{(4\Omega^2 + r\,\partial\Omega^2/\partial r)}$ is the epicyclic frequency [2]. Setting $\mathbf{B} = v_{Az} = 0$ gives the Rayleigh stability criterion, $\kappa^2 > 0$, which is satisfied for our Keplerian disk (the Keplerian value being $\kappa^2 = \Omega^2$). With a magnetic field, instability requires that the quantity $\{\ldots\} < 0$, giving instability if [31]:

$$k_z^2 v_{Az}^2 + r\,\partial\Omega^2/\partial r \leq 0 \quad \text{(C5)}$$

We assume localization to the disk, giving $k_z \geq (\pi/H)$, whereby Eq. (C5) yields the marginal stability condition Eq. (A18) in Appendix A. To show the importance of MRI, we introduce into Eq. (A18) the Standard Model of Ref. [17], adding our magnetic parameters in Eq. (12) and Appendix B, and Keplerian rotation. Ref. [17] gives different results above and below a radius $r_{ab} \equiv 236R_G = 23.6a$ Then Eq. (A18) yields $(\pi/4)(B_z^2/\Sigma H) = 0.9 \times 10^{-12}(a/r)^{4.5} \leq -r\partial/\partial r\,\Omega^2 = 1.5 \times 10^{-9}(a/r)^3$ for $r < r_{ab}$ (with $\Sigma = 3 \times 10^4\,(a/r)^{3/2}$ and $H = 2.6 \times 10^{13}$), and the same result with $(a/r)^{4.5} \rightarrow (a/r)^{2.35}$ for $r > r_{ab}$; hence instability for $r < 2700a = 2.7 \times 10^4\,R_G$ compared to a range of interest $r < 1000R_G$ for the dynamo mechanism of Ref. [17].

We are now ready to calculate MRI transport quantities used in Appendix A. For quasi-linear transport quantities, which are quadratic in the perturbations, we require v_{1z}

and B_{1z} in which k_z is replaced by $\partial/\partial r$ (higher order in $1/k_z r$). These are obtained from $-i\omega B_{1z} = \partial/\partial r\,(-v_{1r}B_z)$, and:

$$-ik_z(v_{1z}B_\phi) - \partial/\partial r\,(v_{1r}B_\phi) \quad = \quad 0 \qquad \text{(C6)}$$

yielding:

$$B_{1z} \quad = \quad (i\omega)^{-1}\partial/\partial r\,(-v_{1r}B_z) \quad = \quad (ik_z)^{-1}\,\partial B_{1r}/\partial r \qquad \text{(C7)}$$

$$v_{1z} \quad = \quad -(ik_zB_\phi)^{-1}\partial/\partial r\,(v_{1r}B_\phi) \qquad \text{(C8)}$$

We first calculate the accretion velocity, using Eq. (C1). For the perturbations above, the z-component of $\langle \mathbf{v_1} \times \mathbf{B_1} \rangle$ is zero, while the toroidal component gives:

$$\begin{aligned} v_r \quad &\equiv \quad \langle v_{2r} \rangle \quad = \quad -\langle (v_{1z}B_{1r} - v_{1r}B_{1z}) \rangle_\phi / B_z \\ &= \quad \langle \mathrm{Re}\{-iv_{1r}\,(B_{1r}/k_z)[(B_\phi^{-1}\,\partial B_\phi/\partial r) - (B_z^{-1}\,\partial B_z/\partial r)]\} \rangle / B_z \\ &\approx \quad -\langle 1/2\,(\omega/k_z^2 r)\,(B_{1r}/B_z)^2 \rangle \end{aligned} \qquad \text{(C9)}$$

In the second line, we use v_{1z} and B_{1z} from Eqs. (C7) and (C8), whereupon terms $\propto \partial v_{1r}/\partial r$ cancel, and we calculate the quantity in […] using the asymptotic limit of the field solution of Appendix B. In the third line, we use v_{1r} from Eq. (C2). As noted earlier, v_r in Eq. (C9) is the only quantity in the accretion model of Appendix A that requires turbulent perturbations for its existence, the reason being that only v_r requires transport perpendicular to **B**. Another quadratic term that arises in taking $\langle \ldots \rangle$ over the mass conservation equation, of the form $\langle \rho_1 v_{1r} \rangle$, is identical to Eq. (C9), so we drop it here.

We can express the turbulence pressure in Eq. (A11) in terms of v_r in Eq. (C9) using $v_{1z} \approx (v_{1r}/ik_z r) = (-\omega/ik_z^2 r)(B_{1r}/B_z)$ from Eq. (C2,C8), giving:

$$P_z \quad = \quad 1/2\rho\langle v_{1z}^2 \rangle \quad = \quad -\alpha_z \rho H v_r \quad = \quad \alpha_z (M^*\Omega/2\pi r)(H/r) \qquad \text{(C10)}$$

where $\alpha_z = (\omega/\Omega k_z^2 H)^2$ is an approximation to the proper average over modes.

Next we compute MRI "hyper-resistive" heating [14], appearing in Eq. (A12). We can calculate this directly in terms of $E_\phi = c^{-1} v_r B_z$ and $j_\phi = -(4\pi)^{-1}(\partial B_z/\partial r)$ giving:

$$(P_{HEAT})_{MRI} = j_\phi[-c^{-1}\langle \mathbf{v}_1 \times \mathbf{B}_1\rangle_\phi] = v_r \, \partial/\partial r \, (B_z/8\pi)^2 \qquad (C11)$$

Eqs. (C10) and (C11) provided closure in Appendix A, without knowledge of perturbation amplitudes, giving results in terms of v_r (or M*). We obtain the amplitudes starting from Eq. (C9), giving;

$$(B_{1r}/B_\phi)^2 = (B_z/B_\phi)^2(B_{1r}/B_z)^2 = (a/r)(-2v_r/r\omega)k_z^2 r^2 = (\pi/5)^2 \approx 1 \qquad (C12)$$

where we use $(B_z/B_\phi)^2 = a/r$ for the asymptotic result from Appendix B; $(-2v_r/r\omega) = 1$ for v_r in Eq. (A21b) with $\omega \approx \Omega_{KEP}$; and $k_z r = (\pi r/H)$ with $H/r = 5\sqrt{a/r})$ from Eq. (A21c). Near marginal stability $B_{1\phi} \approx B_{1r}$ [31], so also $B_{1\phi}/B_\phi \approx 1$. Combining Eqs. (A21d,C7,C12) gives $B_{1z} \approx (k_z r)^{-1} B_{1r} \approx (H/\pi r) B_\phi \approx (a/r)^{1/2} B_\phi \approx B_z$. Thus, all perturbations are comparable to their unperturbed counterparts:

$$(B_{1r}/B_\phi) \approx (B_{1\phi}/B_\phi) \approx (B_{1z}/B_z) \approx 1 \qquad (C13)$$

The corresponding large MRI Torque $\langle - r j_{r1} B_{1z}\rangle$ is merely additive to its 2D counterpart, both serving to extract energy from rotation.

Though such magnitudes marginally violate quasi-linear assumptions, we can get some idea how perturbation amplitudes saturate at the values in Eq. (C13) using quasi-linear energy conservation, given by:

$$\partial/\partial t \, (\Sigma_{\mathbf{k}} B_{1\mathbf{k}}^2/8\pi) = 2i\omega(\Sigma_{\mathbf{k}} B_{1\mathbf{k}}^2/8\pi) + \partial/\partial z \, (\Sigma_{\mathbf{k}}[(\omega/k) B_{1\mathbf{k}}^2/8\pi] \qquad (C14)$$

where $\Sigma_{\mathbf{k}}$ sums over modes and the term on the far right is a damping term due to the perturbed Poynting vector propagating fluctuation energy into the jet. Note that both mean field and perturbation quantities serve to eject angular momentum from the disk, the main difference being that the implied velocity perturbations for the fluctuation-

driven angular momentum should be strongly damped by synchrotron radiation in the jet, perhaps accounting for the intense synchrotron luminosity observed near the disk.

In steady state, Eq. (C14) simply gives $kH \approx \pi$. But the dynamic coupling of Eqs. (C14) and Eq. (A1) contributes to the system stability causing dynamo current I to hover around the steady-state value in Eq. (4). If fluctuations increase too much, mass conservation cuts off the accretion supply. If they decrease too much, Eq. (C14) stores angular momentum that increases the instability producing accretion.

The required MRI fluctuation levels are diminished if an external source of helicity helps sustain the accretion-driven dynamo. The stellar collision model of Refs. [17,18] is such a process, giving the following modification of Eq. (C8):

$$v_r = - H\Omega \{ <B_{1r}B_{1\varphi}/B_{\varphi}^2)>_{MRI} + <\delta B^2/B^2>_{COLLISION} \} \quad (C15)$$

where we take $\omega/k_z = H\Omega$, also characteristic of the stellar collision process active up to $r < 1000R_G$ [17]. Thus δB^2 due to stellar collisions reduces B_1^2 due to MRI required to achieve a given accretion rate M*. According to Ref. [17], this reduction in MRI turbulence should be especially effective at $r < 1000R_G$.

A complete resolution of how dynamos are created by accretion requires ever more sophisticated experiments and computer simulations. Progress to date supports the existence of dynamos, experimentally in Ref. [3], and by computer simulation in Ref. [18] employing the stellar-collision mechanism and in Ref. [38] with helicity injection by a Poynting-Robertson battery. Other simulations focus on the near neighborhood of the black hole [39]. In Ref. [38], the dynamo ejects a jet.

References:

[1] S.A. Colgate and H. Li, Comp. Rend. Physique **5**, 431 (2004).

[2] J.Frank, A. King and D. Raine, *Accretion Power in Astrophysics*, 3rd. Ed. Cambridge University Press, 2002.

[3] S. A. Colgate et al., "High Magnetic Shear Gain in a Liquid Sodium Stable Couette Flow: A Prelude to an α-ω Dynamo," to be published.

[4] Pierre Auger collaboration, Science **318**, 938 (2007).

[5] S. A. Colgate, R. Cen, H. Li, N. Currier and M. S. Warren, Astrophys. J. **598**, L7 (2003).

[6] T. K. Fowler, S. A. Colgate and H. Li, "On the Origin of Ultra High Energy Cosmic Rays," Lawrence Livermore National Laboratory Report, LLNL-TR-414420, July 2, 2009.

[7] T. K. Fowler, "Homopolar Gun for Pulsed Spheromak Fusion Reactors II," Lawrence Livermore National Laboratory report UCRL-TR-204727, June 2004.

[8] B. Hudson et al., Phys. Plasmas **15**, 056112 (2008); references therein.

[9] P. M. Bellan, S. You and S. C. Hsu, Astrophys. Space Sci. **298**, 203 (2005).

[10] M. Nakamura, H. Li and S. Li, Astrophys. J. **652**, 1059 (2006).

[11] R. D. Blanford and R. L. Znajek, Mon. Not. R. astr. Soc. **179**, 433 (1977).

[12] D. C. Montgomery and D. A. Tidman, *Plasma Kinetic Theory*, McGraw-Hill, New York, (1964), Chapter 10.

[13] W.E. Drummond and M. N. Rosenbluth, Phys. Fluids **5**, 1507 (1962).

[14] T. K. Fowler and R. Gatto, Plas. Phys. & Controlled Fusion **49**, 1673 (2007).

[15] D. Lynden-Bell, Mon. Not. R. Astron. Soc. **341**, 1360 (2003).

[16] S. Diehl, H. Li, C. L. Fryer, and D. Raferty, Astrophys. J. **687**, 173 (2008).

[17] V. I. Pariev and S. A. Colgate, Astrophys. J. **658**, 114 (2207).

[18] V. I. Pariev, S. A. Colgate and J. M. Finn, Astrophys. J. **658**, 129 (2007).

[19] C. R. Sovinec, J. M. Finn and D. del-Castillo-Negrete, Phys. Plas. **8**, 475 (2001).

[20] J. D. Jackson, *Classical Electrodynamics*, John Wiley & Sons, New York, Sec. Ed. Chapter 14.

[21] *Fusion* Part 1A, E. Teller, Ed. Academic Press, New York, 1981, Chapter 5 by T. K. Fowler.

[22] G. R. Smith and B. I. Cohen, Phys. Fluids **26**, 238 (1983).

[23] M. Lyutikov and R. Ouyed, Astroparticle Phys. **27**, 473 (2007).

[24] J. Krolik, *Active Galactic Nuclei*, Princeton Series in Astrophysics

[25] *Fusion* Part 1A, Ibid. Chapter 2 by M. N. Rosenbluth and P. H. Rutherford

[26] M. C. Begelman, R. D. Blandford and M. J. Rees, Rev. Mod. Phys. **56**, 255 (1984).

[27] K. C. Steenbrugge, I. Heywood and K. M. Blundell, Mon. Not. R. astr. Soc. **401**, 67 (2010).

[28] M.Uemura, R. Itoh and M. Villata, Nature **463**, 919 (2010).

[29] U. Shumlak, T. K. Fowler and E. C. Morse, Phys. Plasmas **1**, 643 (1994).

[30] N. I. Shakura and R. A. Sunayev, A & A, **24**, 237 (1973).

[31] S. A. Balbus and J. F. Hawley, Rev. Mod. Phys. **70**, 1 (1998).

[32] C. Yu and H. Li, Astrophys. J. **702**, 75, 2009.

[33] R. D. Blanford and D. G. Payne, Mon. Not. R. astr. Soc. **199**, 883 (1982).

[34] D. A. Uzdensky, A. Konigl, and C. Litwin, Astrophys. J. **565**, 1191(2002.

[35] E. B. Hooper, L. D. Pearlstein and R. H. Bulmer, Nuclear Fusion **39**, 863 (1999).

[36] A. H. Boozer, "Plasma Confinement," Encyclopedia of Physical Science and Technology **13**, 1 (1992).

[37] C. C. Hegna and J. D. Callen, Phys. Plasmas **1**, 2308 (1994).

[38] D. M. Christodoulou, I. Contopoulos and D. Kazanas, Astrphys. J. **674**, 388 (2008).

[39] R. Narayan, J. C. McKinney and A. J.Farmer, MNRAS **375**, 548 (2007).

NOTES

Section 1:

Rather than the black hole itself, τ in Eq. (23) could be due to radiation from the reservoir if M_{RES} is a relatively independent body (if $M_{RES} >> M_{BH}$, probably true [5]) which can radiate to the point that its mass comes to be in equilibrium orbit relative to the black hole. Either way, up to a time τ while mass is falling into the black hole, the dynamo radius grows, starting near the black hole and growing for a time τ determined by reservoir and/or central column radiation. In Section 5, this assumption gives the roughly correct jet radius associated with the "active" dynamo radius out to the O-point. The predicted disk radiation at $r < a$ is a fixed fraction of the gravitational power entering the central column (25%), giving an Eddington-limited lifetime.

Section 2:

Eq. (1) The main argument for an electrostatic sheath to eject current is that, given a dynamo with large voltage V, $E = V/d$ for sheath thickness d is the biggest force around. A Poisson's equation evaluating d is given in Appendix A1, Ref. [6].

The argument that electron current cancels in our reference frame fixed in the black hole follows from the fact that both ions and electrons are accelerated, in opposite directions. This would cause their currents to add. However, 2 stream instability tries to flatten the distribution in momentum space. Relavistically, this gives f(v) peaked at the ion speed c and the electron speed – c distributed symmetrically about a minimum at $v = p = 0$, hence zero net electron current.

Eq.(2) This is the standard electrical engineering formulation of energy conservation, given by integrating the energy conservation Eq. (A8) over the volume including the dynamo, the jet, radiolobe and return current in Figure 1. See notes to Appendix A.

Eq. (3) This is just the radial integral of $E_r = c^{-1} r\Omega B_z$

Eq. (4) As stated in the text, the limiting I in a plasma gun (or the accretion disk dynamo which is equivalent) comes from $B_\phi = (2I/ca) = B_z$ near the black hole. This is the

approximate maximum value found in exact spherical self-similar solutions in Refs. [31,32]. In the laboratory spheromak with a flux conserver of fixed size, increasing V can cause the current to grow beyond this limit, until limited by either collisional resistance, or turbulent hyper-resistivity causing relaxation to fill the volume (see Ref. [13]). This "bubbleburst" current threshold is well established by experiments and simulation codes. In the astrophysical case with unlimited volume, the current tries to hover at the threshold (see Section 2 and Appendix B).

Eq. (5), (7), (9) - (11) See text

Eq.(6) $1/2\ \Lambda I^2 \equiv \int_a^R 2\pi rLdr(B_\phi^2/8\pi) = \int_a^R 2\pi rLdr\ (2I/cr)^2(1/8\pi) = (I^2/c^2)L\ lnR/a$

Could add 1 to get (1 + lnR/a) as approximation including r < a (central column) but not important since $lnR/a \approx 20$.

$\Lambda = 2L(lnR/a / c^2)$

Eq. (8) For constant $I = (caB_o/2)$:

$d/dt\ 1/2\ \Lambda I^2 = dL/dt\ [(lnR/a / c^2)(caB_o/2)]I$

$= (1-\alpha_{ACCEL})IV = I(1-\alpha_{ACCEL})[(a\Omega/c)(aB_o)]$

$dL/dt = 2(1-\alpha_{ACCEL})(a\Omega/ln\ R/a)$

Eq. (12) (numbers):

Let $M_{BH} = 10^8\ M_{SUN} = 2 \times 10^{41}$, $\tau = 10^8$ yrs, $M^* = (M_{SUN}/\tau) = 6.7 \times 10^{25}$

$G = 6.7 \times 10^{-8}$, $R_G = (2M_{BH}G/c^2) = (2 \times 2 \times 10^{41} \times 6.7 \times 10^{-8}/9 \times 10^{20}) = 3 \times 10^{13}$

Keplerian: $\Omega_{KEP}(a) = (M_{BH}G/a^3)^{1/2} = [2 \times 10^{41} \times 6.7 \times 10^{-8}/(3 \times 10^{14})^3]^{1/2} = 2.2 \times 10^{-5}$

$a = 10R_G = 3 \times 10^{14}$

For Keplerian rotation ($\Omega < 0$):

$-(a\Omega/c) = [(3 \times 10^{14})(2.2 \times 10^{-5})/(3 \times 10^{10})] = 0.22$

and from Eq. (8), with lnR/a = 20:

$L = -(a\Omega\tau/\ln R/a) = (0.22 \times 3 \times 10^{10} \times 3 \times 10^{15}/20) = 10^{24}$

We calculate $IV = 0.25\, P_{CC}$ from gravitational power P_{CC} deposited in the central column at $r < a$, and ejected with an efficiency 25% (see Appendix A). Gravitational power deposited in a central column occupying $R_G < r < a$ is:

$P_{CC} = M^*[V_G(a) - V_G(R_G)] = M^*(M_{BH}G/R_G)(1 - R_G/a) = (0.95)(1/2\, M^*c^2) = 2.7 \times 10^{45}$ cgs

where $V_G = M_{BH}G(1/R_G - 1/r)$. Then, using Eqs. (3) and (4) with $B_z(a) \equiv B_o$ and for efficiency f:

$IV = [(c/2)aB_o][-c^{-1}(a\Omega\, aB_o] = f\, P_{CC} = f\,(0.9)(1/2\, M^*c^2)$

$(aB_o) = (M^*c)^{1/2}[0.9\, f/(a\Omega/c)]^{1/2} = (6.7 \times 10^{25} \times 3 \times 10^{10})^{1/2}\, [0.9\, f/(a\Omega/c)]^{1/2}$

$= (1.42 \times 10^{18})(0.9\, f/0.22)^{1/2} = \sqrt{f}\, 2.9 \times 10^{18}$

$B_o = (aB_o/a) = \sqrt{f}\,(2.9 \times 10^{18}/3 \times 10^{14}) = \sqrt{f}\, 0.97 \times 10^4$

For f = 0.1 (10% efficiency):

$aB_o = 0.92 \times 10^{18}$, $B_o = 3.07 \times 10^3$

$I = [(c/2)aB_o] = [3 \times 10^{10} \times 0.92 \times 10^{18}/2] = 2.03 \times 10^{28}$ cgs

$\rightarrow 2.03 \times 10^{28} \times (1.6 \times 10^{-19}/4.8 \times 10^{-10}) = 4.57 \times 10^{18}$ amps

$V = [-c^{-1}(a\Omega\, aB_o] = (.22)(0.92 \times 10^{18}) = 0.202 \times 10^{18}$ cgs

$\rightarrow 0.202 \times 10^{18}\,(300 \text{volts/stat}) = 6.06 \times 10^{19}$ volts

For f = 0.25 (25% efficiency), multiply by $\sqrt{(.25/.1)} = 1.58$:

$B_o = 1.58 \times 3.07 \times 10^3 = 4.85 \times 10^3$

$I = 1.58 \times 4.57 \times 10^{18} = 7.22 \times 10^{18}$ amps

$V = 1.58 \times 6.06 \times 10^{19} = 9.57 \times 10^{19}$ volts

Section 3:

Eq. (13) $E_{||}$ is a standard quasi-linear estimate. The limit on the far right is described in the text, using a quasi-linear diffusion coefficient D. The novel feature is the use of free energy conservation to estimate the fluctuation level δB giving:

$$(B_o^2 + \langle \delta B^2 \rangle) R_1^2 = B^2 a^2$$

The right hand side is proportional to the energy per unit length of the central column for $B \propto I$ somewhat above bubbleburst. The left hand side is the energy after turbulent diffusion increases the radius a to $R_1 > a$ and reduces the field back to the bubbleburst level. This is related to helicity conservation in a slightly different formulation in Ref. [6], Appendix A6 showing that it is helicity conservation for the mean field that causes L to increase rather than I in a system of infinite extent. Relaxation driving helicity into the closed flux between the central column and the return current in Figure 1 requires the current to increase above bubbleburst as resistance and hyper-resistivity does in the laboratory [14].

Eq. (14):

Write Eq. (14) as $x = (Dt/a^2)$, $Y = (v_o t/a)$, $G = B_0^2/B^2 < 1$

$1 = (G + x/Y)(1 + x) \rightarrow \quad x^2 + (GY + 1)x = Y(1 - G)$

$x = 0$ if $G = 0$, consistent with the comments above

In general:

$x = 1/2\ (GY + 1)\ \{[1 + 4Y(1 - G)/(GY + 1)^2]^{1/2} - 1\}$

If $G = 1$, $x = 0 << 1$ any Y

If $Y >> 1$, $x \approx (1 - G)/G$ In text we take $G \approx 1$, giving $(1 - G)/G \approx (1 - G) < 1$

If $Y << 1$, there is not enough time for diffusion to occur, which drives D up, the solution $D \propto x \propto 1/\sqrt{Y}$

Eq. (15) See text

Eq. (16) Solve $ecE_{||}$ (heating) $\geq$ $2/3\ (e^2\alpha^2\gamma^4/c^3) = 2/3\ (e^2c\gamma^4/R_C^2)$with centrifufgal $\alpha = c^2/R_C$. The c's cancel giving:

$$\gamma \quad \leq \quad [(3/2)\ E_{||} R_C^2/e]^{1/4}$$

For $E_{||} = \Delta V/L =$ $[(\Delta V/V)(6 \text{ to } 9\ 10^{19})/L\ /300\ (\text{volt/stat})]/L$

$= [0.05(2 \text{ to } 3\ 10^{17}]/10^{24} =$ cgs and $R_C = a = 3 \times 10^{14}$ cm

$\gamma \leq [3/2\ 0.05(2 \text{ to } 3\ 10^{17})10^{-24}(3 \times 10^{14})^2/\ 4.8 \times 10^{-10}]^{1/4} = (0.28 - .42 \times 10^{31})^{1/4}$

$= (2.3\text{-}2.5) \times 10^7$ Energy emerging from central column: not enough

Eq. (17):

$\beta_\perp = (8\pi n_i \gamma m_\perp v_\perp^2/B_\phi^2) = 8\pi\ (I/e\langle v\rangle 2\pi r\Delta)e(\gamma m_i v_\perp^2/B_\phi)(rc/2I)$

$= 2(v_\perp/\langle v\rangle)(\gamma m_i c v_\perp/erB_\phi) = 2(v_\perp/\langle v\rangle)(r_L/r)$

Eq. (18) See text

Eq. (19) DCLC criterion

Relativistic $(\omega_C^2/\omega_C^2) = (e^2B^2/c^2m^2\gamma^2)(m\gamma/4\pi ne^2)$

$= (v_\perp/c)^2(2B^2/8\pi nm\gamma c^2) = 2(v_\perp/c)^2(1/\beta_\perp)$

Section 4:

Eq. (20): $N(E) = \int_a^R dr \int_0^H dz\ (-D\ \partial^2F(r,zE)/\partial z^2) = \int_{R(E)}^R dr\ (I/e\langle v\rangle)\ f(E)\ (\kappa^*D/\Delta^2)$

The first integral is axial transport out of the nose.

For the second simplified form, see text.

Eq. (21):

Change variable $r \rightarrow E(r) = (eV/\ln R/a)\ln(r/a)$

Limits: R becomes $E(R) = eV$, $R(E) = E(R(E)) = E$. (See Notes on file, Ref. [6])

Let: $\langle v\rangle = D/r \qquad V = (a\Omega/c)aB_0 = 0.2\ aB_0$

$\Delta(r) = (m_i\gamma c v_r/eB_\phi)$ (with $v_r \approx c$) $\approx r(E(r)/eB_o a) = 5\ r\ (E(r)/eV)$

$dr = dE(r)[1/dE(r)/dr] = dE(r)(r/eV)\ln R/a$

$dr\ (D/\langle v\rangle\Delta^2) = dE(r)(r/eV)\{(r/D)(D/[5r(E(r)/eV)]^2\}$

$= dE(r)\ E(r)^{-2}\ (eV/r^2)$ independent of r, D

$f(E) = 1/E(r)$

$N(E) = \int_{R(E)}^R dr\ (I/e\langle v\rangle)\ f(E)\ (\kappa^*D/\Delta^2)$

$= (I/e)(\kappa^*\ln R/a)\int_E^{eV} dE(r)(r/eV)(I/e)(r/D)\ f(E)(D/[5r(E(r)/eV)]^2)$

$= (I/e)\ \kappa \int_E^{eV} dE(r)\ (eV/E(r)^2)\ f(E)$, $\kappa = (\kappa^*\ (\ln R/a)/25)$

Eq. (22): To calculate κ using Eq. (21): $(eV/E_2) = 9000$

$$IV = \int dE\, E\, N(E) = (I/e)\, \kappa \int_{E2}^{eV} dE\, E[(eV)^{1.7}/E^{2.7}]$$

$$= \kappa(I/e)(eV)(1/0.7)[(eV/E_2)^{0.7} - 1] = \kappa IV(1/0.7)[(9000)^{0.7} - 1]$$

$$\kappa = \{(0.7)[(9000)^{0.7} - 1]\}^{-1} = 1.19 \times 10^{-3}$$

Comment on recycling from the ambient pressure wall at the nose:

$$I_{RECYCLE} = \int_{E2}^{eV} dE\, N(E) = (I/e)\, \kappa \int_{E2}^{eV} dE\, [(eV)^{1.7}/E^{2.7}]$$

$$= \kappa(I/e)(1/01.7)[(eV/E_2)^{1.7} - 1] = I\,(1.19 \times 10^{-3})(1/1.7)[(9000)^{1.7} - 1]$$

$$= 3.69 \times 10^{3}\, I$$

Section 5:

Eqs. (23) – (27) See text and references

Eq. (28)

$$dr/dt = v_r = - c\,(R_G/2r)^{1/2} \quad \text{from Eq. (A21b)}$$

$$2/3\, dr^{3/2}/dt = - c\,(R_G/2)^{1/2}$$

$$r = [R_o^{3/2} - ct\,(R_G/2)^{1/2}]^{3/2}$$

$$R_o = - \int_0^{\tau} dt\, v_r = - \int_0^{\tau} dt\, [- c\, [R_G/2([R_o^{3/2} - ct\,(R_G/2)^{1/2}]^{3/2})]^{1/2}$$

$$\approx \int_0^{\tau} dt\, c\,(R_G/2R_o)^{1/2} \approx c\tau\,(R_G/2R_o)^{1/2}$$

In the next to last paragraph:

$$\lambda_{SYN} = (2\pi/k) = (2\pi c/\omega_{Ce}) = [2\pi c/(eB/m_e\gamma_e c)]$$

$$= [2\pi \times (3 \times 10^2) \times 0.9 \times 10^{-27}\ gm/4.8 \times 10^{-10}](\gamma_e/B) = 1.06 \times 10^4\,(\gamma_e/B)$$

Appendix A

See THIN DISK MODEL assumptions below

Collisionality: see end of this section of notes

Eq.(A1)-(A6) Textbook

Eq. (A7) This is r x ϕ-component of Eq. (A2) with $v_\phi = r\Omega$

Left hand side $\leftarrow = 0 \rightarrow$ $\leftarrow$ r x ϕ-component of Eq. (A2)

$\partial(\rho r v_\phi)/\partial t + \nabla\cdot\rho\mathbf{v}rv_\phi = rv_\phi[\partial\rho/\partial t + \nabla\cdot\rho\mathbf{v}] + r\rho[\partial v_\phi/\partial t + r^{-1}\mathbf{v}\cdot\nabla rv_\phi]$

Right hand side $\leftarrow = 0\rightarrow$

$-\nabla\cdot\mathbf{j}\psi = -j_z\partial(\psi/2\pi)/\partial z - j_r r^{-1}\partial(\psi/2\pi)/\partial r + \psi\nabla\cdot\mathbf{j}$

$= r[j_z B_r - j_r B_z\}]$ r.h.s. r x ϕ-component of Eq. (A2)

Eq. (A8) $(4\pi)^{-1}\,\mathbf{B}\cdot$ Eq. (A4)

$(4\pi)^{-1}B\,\partial B/\partial t = -(4\pi)^{-1}c\,\mathbf{B}\cdot\nabla x\mathbf{E} = -c\,\nabla\cdot(\mathbf{E}x\mathbf{B}/4\pi) - c\,\mathbf{E}\cdot(\nabla x\mathbf{B}/4\pi)$

$= -c\,\nabla\cdot(\mathbf{E}x\mathbf{B}/4\pi) - \mathbf{j}\cdot\mathbf{E}$

$\mathbf{v}\cdot$ Eq. (A2)

$v\rho\partial v/\partial t + \mathbf{v}\cdot[\rho\mathbf{v}\cdot\nabla\mathbf{v}] = \mathbf{v}\cdot c^{-1}\mathbf{j}x\mathbf{B} + \mathbf{v}\cdot\mathbf{F} = -\mathbf{j}\cdot c^{-1}\mathbf{v}x\mathbf{B} + \mathbf{v}\cdot\mathbf{F}$

$= \mathbf{j}\cdot\mathbf{E} + \mathbf{v}\cdot\mathbf{F}$ using Ohm's Law

Eq.(A3) $\partial(3nkT)/\partial t = P_{HEAT} - P_{RAD}/H$ neglecting heat flu

Adding cancels $\mathbf{j}\cdot\mathbf{E}$, giving Eq.(A8)

THIN DISK MODEL:

Eq. (A9) Definition of M*, taken as constant (see text)

Eq. (A10) Integrate Eq. (A7) over $\int_0^H 2\pi r dz$ using Eq. (A9). L.h.s. as in text.

Eq. (A11) l.h.s. is $\int_0^H dz\rho(-\nabla[MGz/(r^2 + z^2)^{3/2}]$ with $z/(r^2 + z^2)^{3/2} \approx z/r^3$ (see [2],Chap.5)

Eq. (A12) This is $P_{HEAT} - P_{RAD}/H = 0$

Eqs. (A13, 14, 15)

In-text integral shows the jet power is Ω x jet ang. mom.

The cancellation giving Eq. (A15) follows using Eq.(A10) with $\nu = 0$

THIN DISK MODEL ASSUMPTIONS:

The cancellations in Eq. (A15) are only exact for the 1D equations given by integrating 2D equations over the disk height H (the "thin disk approximation" [2]). In 2D the thin disk approximations are:

1. We set $B_r = 0$ inside the disk as it is in the force-free jet so they match. To preserve div$\mathbf{B} = 0$ this requires B_z constant in z. However:

$$\partial B_\phi/\partial z = -(4\pi/c) j_r \neq 0$$

so our asymptotic field solution of Eq. (A19g), $B_z \propto \Omega$, is some kind of z average <…>:

Integrating (A19g) gives:

$$\langle B_z^2 \rangle = -\int_0^2 dr\, r^{-2} \partial(r^2 \langle B_\phi^2 \rangle)/\partial r$$

and angular momentum conservation can be written as

$$\langle B_z \rangle = -\langle c r^{-1} \partial/\partial r(r\rho v_r r v_\phi)/r j_r \rangle$$

2. Otherwise the approximations giving the 1D model are:

<u>For the Standard Model:</u>

For whatever viscous force $\mathbf{F}_T$ that applies the torque getting rid of angular momentum, in quasi-steady state :

$$\underline{z}\cdot\mathbf{r} \times \mathbf{F}_T = r (F_T)_\phi = r^{-1} \partial/\partial r [r\rho v_r r v_\phi]$$ rate of arrival of angular momentum

Associated power $v_\phi (F_T)_\phi = v_\phi r^{-2} \partial/\partial r [r\rho v_r r v_\phi]$

$$= r^{-2} [(r\rho v_r) v_\phi + (r\rho v_r) r \partial v_\phi/\partial r + r v_\phi \{\partial(r\rho v_r)/\partial r\}]$$

$$= \rho[(\mathbf{v}\cdot\nabla)\mathbf{v}]_\phi + r^{-2} [r v_\phi \{\partial(r\rho v_r)/\partial r\}] \qquad (*)$$

If all mass accretes, the model approximates $\{\partial(r\rho v_r)/\partial r\} = 0$ at all z within the disk. Then $v_\phi (F_T)_\phi = \rho[(\mathbf{v}\cdot\nabla)\mathbf{v}]_\phi$ steady-state energy conservation equation becomes:

$$0 = \mathbf{v}\cdot\mathbf{F} + P_{RAD}/H = v_r[F_r + (F_T)_r] + P_{RAD}/H \qquad (**)$$

$$F_r = -\rho[(MG/r^2) - r\Omega^2 + 1/2\, \partial v_r^2/\partial r]$$

The viscous term $(F_T)_r$ and and v_r in v_r are small ($v_r \propto$ viscosity $\propto c_S$, sound speed), but since nominally P_{RAD} equals gravitational power in the Standard Model, Ω can only be near-Keplerian to the extent that this is not quite true, the actual value being undertermined, and the magnetic field

has been assumed small. But given a dynamo field with poloidal cyclotron frequency > the viscous "collision frequency" c_S/H (sound speed), the Standard Model disk is unstable to MRI, leading to our modified model.

<u>For our modified model:</u>

Viscosity is replaced by $\mathbf{F}_T = c^{-1}\,\mathbf{j}\mathrm{x}\mathbf{B}$ again giving (*) above, but $v_r(F_T)_r$ giving viscous dissipation is replaced by the Poynting vector ejecting power into the jet:

$$\partial/\partial z\,(v_\phi B_z B_\phi/4\pi) = v_\phi B_z \partial/\partial z(B_\phi/4\pi) + (B_\phi/4\pi)\{\partial/\partial z\,(v_\phi B_z)\}$$
$$= -\,c^{-1} j_r (v_\phi B_z) + (B_\phi/4\pi)\{\partial/\partial z\,(v_\phi B_z)\}$$

Dropping the term in {…} (as we do in averaging over the disk height), this shows that, like the viscous counterpart, the Poynting vector also contains $(F_T)_\phi = -\,c^{-1} j_r B_z$ so also (**) holds. But now we can show after the fact that radiation can be dropped, so (**) implies $F_r = 0$, Eq. (A17), and we have a precise MRI-derived formula for v_r, Eq. (A19b), so the model is fully closed including the magnetic field, giving v_r near Keplerian (i.e. "free fall").

3. The above cancellation says that, ignoring radiation, energy conservation gives:

$$v_r F_r + \{v_z\} F_z = 0$$

where again dropping the term in {..} gives our 1D model

So our thin disk model giving a perfect match of the field inside the disk to that in the jet assumes that, inside the dynamo:

$$B_r = v_z = \partial/\partial z\,(v_\phi B_z) = \partial/\partial r(r\rho v_r) = 0$$

The toroidal field inside the dynamo satisfies:

$$\partial B_\phi/\partial z = -\,(4\pi/c) j_r \neq 0$$

but in the axial pressure balance matching gravitation to pressure we drop

$j_r B_\phi$ which is first a pinch force near z = 0, then an expulsive force promoting bubbleburst, and finally nil at the disk boundary where $j_r = 0$ in steady state.

Eq.(A16) This is the full expression for the radial force F_r including gravity, centrifugal force and convective r derivative (from $\mathbf{v}\cdot\nabla\mathbf{v}$). $F_r = 0$ by the arguments in text at Eq.(A13).

Eq. (A17) Radial force balance given Eq. (A16)

Eq. (A18) MRI – as in text – with $k_z = (\pi/H)$

Eq. (A19) Reshuffle of Eqs. (A9 - A12) and (A16 – 18) as in text.
From Eq. (A9), $M^* = - 2\pi r\Sigma v_r$, rewritten as Eq. (19c).
Substituting Eq.(A9) into Eq. (A11) (dropping thermal and radiation pressure) gives:
$1/2\ \Sigma H(M_{BH}G/r^3) = 1/2\ \Sigma H\Omega_{KEP}^2 = (\alpha_z M^*\Omega/2\pi r)(H/r) = - (\Sigma H v_r\Omega/r)$
Solving for v_r gives Eq. (A19b).

Eq. (A20) Introducing Eq. (A19b) into Eq. (19a) with $\Omega_{KEP}^2 = C_{KEP}/r^3$ and $\Omega^2 = C/r^K$ and $X = (C/C_{KEP})^2$, we obtain:

$$0 = \Omega_{KEP}^2 - \Omega^2 - (1/8\alpha_z^2)\, r^{-1}\partial[(r\Omega_{KEP}^2)^2/\Omega^2)]/\partial r$$
$$= \Omega_{KEP}^2\{r^{-3} - X\, r^{-K} + [(K-4)/8\alpha_z^2 X]\, r^{-(6-K)}\}$$

Solution: $3 = K = 6 - K \rightarrow K = 3$; $1 - X + [(3-4)/8\alpha_z^2 X] = 0$ giving

$$X^2 - X + (1/8\alpha_z^2) = 0 \rightarrow X = 1/2\ \{1 +/- \sqrt{[1 - (1/2\alpha_z^2)]}\}$$

Let $\alpha_z^2 = 1/2$ (see text). Then X = 1/2.

Eq. (A21): $\Omega = - \Omega_{KEP}\sqrt{X} = - (1/\sqrt{2})\ \Omega_{KEP} = - 0.7\ \Omega_{KEP}$ Eq. (A21a)

$v_r = - 1/2\ r(\Omega_{KEP}^2/\alpha_z\Omega) = - - 1/2\ r(\Omega_{KEP}^2/0.7 \text{ x } 0.7\ \Omega_{KEP}) = - r\Omega_{KEP}$ Eq. (A21b)

Using numbers above (Section 2 notes):

By Eq. (A19c):

$\Sigma = -(M^*/2\pi r\, v_r) = -\,[6.7 \times 10^{25}/2\pi \times (3 \times 10^{14})^2\,(r/a)^2 \times (2.2 \times 10^{-5})(a/r)^{3/2}\,]$

$\Sigma = 5\,\sqrt{(a/r)}$ Eq.(A21c)

By Eq. (A19d), with constant $I = (caB_o/2)$ and $B_z = B_a(a/r)^{3/2}$ we obtain at r = a:

$(IB_z/c) = (aB_a^2) = -\,M^*[r^{-1}\partial/\partial r\, r^2\,\Omega]_a = M^*c\,(1/2\; a\Omega/c)$

Multiply by a, giving result similar to central column in Section 2:

$(aB_a) = [M^*c(1/2\; a\Omega/c)]^{1/2} = 1.4 \times 10^{18}\,(1/2 \times 0.7 \times 0.22)^{1/2} = 4 \times 10^{17}$

$B_a = (4 \times 10^{17}/3 \times 10^{14}) = 1.33 \times 10^3$

Why this value is less than the average central column value in Eq. (12) is discussed in Appendix A.

Given $B_z = B_a(a/r)^{3/2} = 1.33 \times 10^3(a/r)^{3/2}$, we can calculate H from Eq. (A19e):

$H/a = (\pi/4\Sigma)[B_z^2/(-r\partial\Omega^2/\partial r]/a = (\pi/4\Sigma)(B_z^2/3\Omega^2)/a$

$= [\pi/4 \times 5\,\sqrt{(a/r)}][(1.3 \times 10^3)^2/(3 \times (2.2 \times 10^{-5}/\sqrt{2})^2(3 \times 10^{14})]$

$= 0.65\,\sqrt{(r/a)}$ Eq. (A21d)

Also using B_z , H and v_r above in Eq. (19f) gives T. We set $\tau_{OP} = 1$ (see text), and $\sigma = 5.7 \times 10^{-5}$ giving:

$T = [Hv_r(\partial(B_z^2/8\pi)/\partial r)/\sigma]^{1/4} = \{[H/r][-v_r][3(B_z^2/8\pi)](1/\sigma)\}^{1/4}$

$= \{[(0.65\,(a/r)^{1/2}][0.7(3x10^{14})(2.2 \times 10^{-5})(a/r)^{1/2}]$

$\times\; [(3(1.3 \times 10^3)^2(a/r)^3/8\pi\; x(5.7 \times 10^{-5})\}^{1/4}$

$\rightarrow \quad T = \{\,0.106 \times 10^{20}\}^{1/4}(a/r)$

$= 5.7 \times 10^4(a/r)$ Eq. (A21e)

Eq. (A22) From the IV derivation:

$a^2 = M^*c(1/B_0^2)[f/(a\Omega_{KEP}/c)]$

From the asymptotic solution:

$a^2 = M^*c(1/B_a^2)(a\Omega/c)] = 0.7\; M^*c(1/B_a^2)(a\Omega_{KEP}/c)$

Equating these expressions using $(a\Omega_{KEP}/c) = (R_G/2a)^{1/2}$ gives Eq. (A22).

Whether black body or not, the surface radiated power equals the MRI-derived heating power given by:

$$P_{RAD} = - Hv_r \partial(B_z^2/8\pi)/\partial r = (0.46a(r/a)^{1/2})(r\Omega)[(3B_o^2(a/r)^3/r]$$
$$= \Omega(B_o^2 a)\,[1.38\,(a/r)^{7/2}]$$

The justification for neglecting radiation (except to calculate T) comes from a comparison with the Poynting vector power:

$$\Omega(IB_z/c) = \Omega(B_o^2 a)[1/2\,(a/r)^{3/2}]$$
$$= 0.7 \times (2.2 \times 10^{-5})[(1.3 \times 10^3)^2 \times 3 \times 10^{14}/2](a/r)^3$$
$$\Omega(IB_z/c) = 3.9 \times 10^{15}\,(a/r)^3$$

Thus radiation, omitted in deriving the key equation Eq. (19a), is asymptotically small as assumed.

Similarly, the thermal and radiative pressures can be ignored. The thermal pressure is:

$$nkT = (\Sigma/Hm_i)kT = [(7.6(a/r)^{1/2})/0.5a(r/a)^{1/2}m_i][k \times 0.52 \times 10^5(a/r)]$$
$$= [(7.6/0.5 \times 3 \times 10^{14} \times 1.7 \times 10^{-24})][(1.4 \times 10^{-16} \times 0.52 \times 10^5](a/r)^2$$
$$= 0.02\,(a/r)^2$$

The radiation pressure is:

$$P_{RAD}/c = [0.4 \times 10^{15}\,(a/r)^4 / 3 \times 10^{10}] = 1.33 \times 10^4\,(a/r)^4$$

The axial pressure balancing gravity is (Eq. (A11):

$$P_z = 1/2\,\Sigma H\Omega_{KEP}^2$$
$$= 1/2\,[7.6(a/r)^{1/2}]0.5(3 \times 10^{14})(r/a)^{1/2}][(2.2 \times 10^{-5})^2(a/r)^3]$$
$$= 2.8 \times 10^5\,(a/r)^3$$

Thermal pressure could perhaps compete at $r = a(2.8 \times 10^5/0.02) \approx 0.1R_{JET}$.

Collisions:

Collisions matter only to maintain a fully ionized plasma in the disk. Accreting material probably enters the dynamo already ionized. Any neutrals entering by the shortest path = H would be ionized if, for ionization cross section $\sigma_{ion} > 10^{-16}$:

$(\Sigma\sigma_{ion}/m_i) > [7.6\,(a/r)^{1/2}/1.7 \times 10^{-24}]\,10^{-16} >> 1$ surely true

The disk ion density, collision frequency and cyclotron frequency are:

$n = (\Sigma/m_i H) = [5 (a/r)^{1/2}/1.7 \times 10^{-24}]/(0.7(r/a)^{1/2} 3 \times 10^{14}] = 1.4 \times 10^{10}(a/r)$

$\nu_{COLL} = [n/(10^{10} T_{KeV}^{e/2})] = [1.4 \times 10^{10}(a/r)/(10^{10} T_{KeV}^{e/2})] = 1.4 [(a/r)/T_{KeV}^{e/2})]$

for T in KeV

$\omega_C = (eB_\phi /m_i c) = [4.8 \times 10^{-10} \times 3 \times 10^3 (a/r)/1.7 \times 10^{-24} \times 3 \times 10^{10}] = 2.8 \times 10^7 (a/r)$

Then the plasma is "magnetized" ($\nu_{COLL} << \omega_C$) giving diffusion coeffients $D \propto r_L^2$

Numbers are like laboratory plasmas (but lower than typical density) so that D is irrelevant on astrophysical dimensions

The density $n \propto j_\phi \propto r^{-5/2}$. Integrating gives the density in the Central Column = about 2 sun Masses (neglibible).

Appendix B

See FLUX MAPPING, Time-Dependent Grad-Shafranov Eq. below

Eq. (B1) Derived from Eq. (A19g) using $I = (c/B_z)(M^* r^{-1} \partial/\partial r\, r^2\Omega)$

from Eq. (A10) with $\nu = 0$

$\partial/\partial r\, B_z^2 + r^{-2}\partial/\partial r\, (2I/c)^2$

$= \partial/\partial r\, B_z^2 + r^{-2}\partial/\partial r\, (2M^* r^{-1}\partial/\partial r\, r^2\Omega/B_z)^2 = 0$

$\partial/\partial r\, B_z^2 + r^{-2}\partial/\partial r\, (g/B_z^2) = 0$

Eq. (B2) $g = (2M^* r^{-1}\partial/\partial r\, r^2\Omega)^2$

Eq. (B3) Multiply Eq. (B1) by $2B_z^2$. Let $\Omega^2 \propto r^{-K}$ giving $g \propto r^{-K}$ and $\partial g/\partial r = -K(f/r)$.

$\partial(r^2/g)/\partial r = r^{-1}(K+2)(r^2/g)$ etc. Eq. (B1) becomes:

$2B_z^2[\partial/\partial r\, B_z^2 + r^{-2}\partial/\partial r(f/B_z^2)]$

$= \partial B_z^4/\partial r + 2B_z^2[- r^{-2} g\, B_z^{-4}\partial B_z^2/\partial r + (rB_z)^{-2}\partial g/\partial r] = 0$

$\partial B_z^4/\partial r\, [1 - (g/r^2 B_z^4)] = -2r^{-2}\partial g/\partial r = 2\, r^{-1} K(g/r^2)$

Change variable to $F = (B_z^4 r^2/g)$ (dimensionless)

$\partial F/\partial r = (r^2/g)\partial B_z^4/\partial r + B_z^4\partial(r^2/g)/\partial r = (r^2/g)\partial B_z^4/\partial r + r^{-1}(K+2)(r^2 B_z^4/g)$

$\partial B_z^4/\partial r = (g/r^2)[(\partial F/\partial r) + r^{-1}(K+2)F]$

Substitute into (from above):

$\partial B_z^4/\partial r\,[1 - (g/r^2B_z^4)] = 2\,r^{-1}K(g/r^2)F + (K-2)]^p$

Test by taking dx/dF and inverting:

$dx/dF = -\,kF^{-(k+1)}\,[(K+2)F + (K-2)]^p + p(K+2)F^{-k}[(K+2)F + (K-2)]^{p-1}$

$= F^{-(k+1)}[(K+2)F + (K-2)]^{p-1}\{p(K+2)F - k[(K+2)F + (K-2)]\}$

$dF/dx = [F^{-k}[(K+2) + (K-2)]^p]^{-1}[(K+2) + (K-2)][p(K+2)F - k[(K+2)F + (K-2)]^{-1}$

$= x^{-1}[(K+2)F + (F-2)]\,(F/\,[(K+2)(p-k)F - k(K-2)])$

This recovers Eq. (B3) if:

$k(K-2) = 1 \rightarrow k = 1/(K-2)$

$(K+2)(p - k) = (K+2)[p - (1/(K-2))] = 1$

$\rightarrow p = [(K-2)(K+2)]^{-1}[(K+2) + (K-2)] = 2K/(K^2-4)$

Eq. (B5) Definition of λ

Eq. (B6) - (B8) See text.

Eq. (B9):

This shows that internal kink modes are stable in the diffuse pinch but can occur in the central column and probably drive $E_{||}$ with saturation at $\delta B/B = 10^{-6}$ (text after Eq. (13)).

External kinks give much weaker $\delta B/B$. For growth $\xi \approx R$ over 50 growth times (Eq. (27)):

$\xi(z=0) = R[R\exp(-50)] = 2 \times 10^{-22} R$

$\xi(z) = \xi(z=0)\exp(50z/L) \rightarrow R$ at $z = L$

$\delta B = (k_z\xi)B = (2\pi/L)\,2 \times 10^{-22} \exp(50\,z/L)$

$\delta B/B$(external) $< 10^{-6}$(internal) if $z < .7L$.

$\delta W = \int_0^L dz\,\xi^2(B_o a/R)^2 q(R)$

$= \int_0^L dz[R \exp(-50) \exp(50z/L)(B_o a/R)]^2(2\pi R/L)(a/R)^{1/2}$

$= L(B_o a)^2\,(a/R)^{1/2}\,(2\pi/50)\int_0^{50} dx \exp(-x) \qquad x = 50\,(1 - z/L)$

$= (0.2 \times 4/\ln R/a)(a/R)^{1/2}\,[1/2I^2\Lambda]$

$\delta W \quad < \quad 4 \times 10^{-6} [1/2 I^2 \Lambda]$

using $\langle R/a \rangle > 10^8$, $B_o a = 2I/c$, $\Lambda = 2Lc^{-2} \ln R/a$, $\ln R/a = 20$

Comments on particle dynamics, text after Eq. (B8):

1. In Sagitta approximation, minimum Larmor radius to keep ion on field line is:

$r_L/d = d/R_C$ for curvature radius R_C and $d = v_{||}/\omega_C$ (forward travel along field line during one cyclotron period) and $r_L = v_\perp/\omega_C$ with $\omega_C = (eB/m\gamma c)$.

$r_L = v_\perp/\omega_C = d^2/R_C = (v_{||}/\omega_C)^2/R_C$

Magnetic moment $\mu = m\gamma\, r_L v_\perp = m\gamma\, (r_L^2 \omega_C) = [(m\gamma v_{||})^4/(eB)^3 R_C^2]$ – increasing as $\gamma v_{||}$ increases during acceleration

2. Drifts in nose return current channel

$$\mathbf{j} = - \underline{\mathbf{r}}(\partial B_\varphi/\partial z) + \underline{\mathbf{z}}(\partial B_\varphi/\partial r + B_\varphi/r)$$

$$\mathbf{v}_D = 1/2\, v_\perp r_L B^{-2} (\mathbf{B} \times \nabla B) \qquad B \text{ is magnitude of } \mathbf{B} \qquad [25]$$

$$= 1/2\, v_\perp r_L\, B^{-1} [(\underline{\mathbf{r}}\, \partial B_\varphi/\partial z) - \underline{\mathbf{z}} \partial B_\varphi/\partial r\,]$$

$$\mathbf{v}_D \times \mathbf{j} = - \underline{\boldsymbol{\phi}}\, 1/2\, (B_\varphi/B)\, v_\perp (r_L/r)\, \partial B_\varphi/\partial z$$

Note that, applied to the central column where $\partial B_\varphi/\partial z = 0$, $\mathbf{v}_D \times \mathbf{j} = 0$ showing that there are no drifts perpendicular to **j**; drifts are along z doing no harm. Applied to the nose where $\partial B_\varphi/\partial z \approx - B_\varphi/H$ there is a drift component perpendicular to **j** (due to the B_φ/r term in **j**) which ejects ions just as DCLC does. On first sight, drifts and DCLC transport out of the nose are comparable:

$(v_D)_{DRIFT} \approx 1/2\, (r_L/\Delta) v_\perp \approx 1/2\, v_\perp$

$(v_D)_{DCLC} \approx v_\perp$

However drifts are one way while DCLC transport can transport cold ions in (due to positive dn/dz in ambient pressure front) but hot ions out. The recycling influx of cold ions, calculated in our model by the adjusting the parameter κ in Section 4 to conserve energy, is an essential feature allowing **j** to be sustained despite the hot ion loss.

Figure 4: pillbox-0302.pdf file

Corsica Pill Box solution of $\nabla \times \mathbf{B} = \lambda \mathbf{B}$

Rewritten as Grad-Shafranov equation.

For the case in Figure 4, ratio of confined toroidal current to the total, $(\Delta I_\psi/I_\psi) = 13\%$ found by trial and error starting from a boundary condition that $\psi = 0$ up the axis, at the top and down the outer boundary, and $\psi(r,0)$ at $z = 0$ given by:

$\psi(0,z) =$ $\psi(L,r) =$ $\psi(R,z) =$ 0

$\psi(r, 0) =$ $\sqrt{r} \exp(-0.1r)[1 - \exp(-r^{3/2})]$

which gives B_z about flat for $0 < r < 1$ (central column), $B_z = 0$ at $r \approx 10$, and $B_z \propto r^{-3/2}$ from $1 < r < 10$ to match the asymptotic B_z in Figure 3. We could not reproduce exactly the corresponding asymptotic $\lambda(\psi) \propto \psi^{-3}$ using the fitting formula in Corsica of the form $\Sigma a_n x^n$ where $x = (1 - \psi/\psi_{MAX})$. Fig. 4 was derived from a single term $\lambda = a_4 x^4$ where Corsica adjusts a_4 as the total toroidal current is varied at fixed ψ at the boundary. For the reduced dimensions and fixed gridding of Corsica, we were unable to get solutions making the corresponding j_z as steep as it should be, which caused B_r to be non-zero in the range $0 < z < 10$ (on sscale $z = 0$ to 240). Yet the diffuse pinch flux surfaces were straight as expected above $z = 10$. To obtain Figure 4, we kept the $\lambda = a_4 x^4$ but altered the boundary condition so that $\psi(r,0) = \psi(r,-120)$ (as caculated) from $0 < r < 10$ (approximately) matched to the above formula for $r > 10$. This then gave Figure 4 with $B_r = 0$ and straight surfaces for $r < 10$ -- the expected result.

FLUX MAPPING ("Flux Winding"), Helicity Injectionm, Time-Dependent Grad-Shafranov equation, Corsica

1. Solving $\nabla x\mathbf{B} = \lambda\mathbf{B}$ is the correct way to do quasi-static evolution of the field, the same procedure as that applied approximately by Lynden-Bell in Ref. [15] who talks about "winding" but actually solves equilibria.
The problem is that solving $\nabla x\mathbf{B} = \lambda\mathbf{B}$ requires knowing the boundary.
This requires coupling Faraday's Law and the momentum equation.

Equilibria neglect the convective derivative d**v**/dt. When **v** is Alfven speed >> dL/dt, one can set d**v**/dt = 0 giving a quasi-static field. But this does not determine the boundary.

For ideal MHD, the energy equation and helicity equation derived from Faraday's Law have the same content, though for $B_z \propto r^{-3/2}$ and $B_\phi \propto r^{-1}$ the energy is concentrated near the central column whereas (like angular momentum) the helicity is not. The equations come from:

$$\partial/\partial t(\mathbf{B}\cdot\mathbf{B}/8\pi) = -c\nabla\cdot(\mathbf{E}\times\mathbf{B}/4\pi) - \mathbf{j}\cdot\mathbf{E} \qquad \text{energy}$$

$$\partial/\partial t(\mathbf{A}\cdot\mathbf{B}/8\pi) = -c\nabla\cdot(\mathbf{E}\times\mathbf{A}) - \mathbf{B}\cdot 2\nabla\phi \qquad \text{helicity}$$

where $\mathbf{j} \propto \nabla\times\mathbf{B}$ so the energy equation depends only on **E** and **B** and $\mathbf{B} = \nabla\times\mathbf{A}$ so that the helicity equation depends only on **E** and **A**. For helicity, we use $\mathbf{E} = -\nabla\phi - c^{-1}\partial\mathbf{A}/\partial t$ and for ideal MHD, $\mathbf{E}\cdot\mathbf{B} = 0$ (or with turbulence, if the above are "mean" fields $\langle\mathbf{E}\cdot\mathbf{B}\rangle$ is hyper-resistivity that can transport helicity between mean field flux surfaces but not out of the box if the box is a flux-conserver). The momentum equation provides $\mathbf{E} = -c^{-1}\mathbf{v}\times\mathbf{B}$ and also $\nabla\phi$ if the external voltage source is a dynamo (homopolar generator), otherwise a capacitor bank. For energy, the Poynting vector propagates power out of the dynamo and through the jet, while the $(\mathbf{E}\times\mathbf{A})$ propagates helicity. The energy source is $\mathbf{j}\cdot\mathbf{E}$. For dynamos, the helicicty source is $\mathbf{B}\cdot 2\nabla\phi$ [Boozer, Ref. [34] in Feb. 9 short version draft].

The Thin Disk model fixes asymptotic values:

$$B_z(r) = B_0(a/r)^{3/2}\ ;\ \Omega(r) = \Omega_0(a/r)^{3/2}\ ;\ B_\phi(r) = B_0(a/r)$$

For a flux surface width Δ, and using $2\pi r A_\phi = \psi$ (real flux) and the fact that $A_\phi B_\phi$ dominates the helicity K (as B_ϕ dominates the energy, or inductance):

$$\delta\psi = (2\pi r\Delta\, B_z(r)) = 2\pi a\Delta\, B_0\,(a/r)^{-1/2}$$

$$\delta K \quad \approx \quad L(r) \int_r^{r+\Delta} 2\pi r dr \, (A_\phi B_\phi) \quad = \quad L(r)\psi a B_\phi \ln[(r+\Delta)/r]$$

where we have assumed flux surfaces are straight as in our model. Then, using Boozer's result above, $dK/dt = 2V\psi$ giving for a single flux surface:

$$d/dt\,(\delta K) \quad = \; dL(r)/dt\; \psi a B_\phi \ln[(r+\Delta)/r] \; = 2\delta\psi\delta V \; = \; 2\delta\psi(\Omega\psi/2\pi)$$

where $\delta V = (\Omega\psi/2\pi)$ is the voltage drop between footprints derived in my previous memo (now with 2π that I now retained in ψ). Then, using $\ln[(r+\Delta)/r] \approx \Delta/r$:

$$dL(r)/dt \; = \; \{2\delta\psi/aB_\phi \ln[(r+\Delta)/r]\}(\Omega(r)/2\pi) \; \approx \quad 2(a\Omega_0)(r/a)^{1/2} \quad = \quad 0.4c(r/a)^{1/2}$$

for $(a\Omega_0) = 0.2c$ in Eq. (16) of the Feb. 9 draft.

Thus, with no other constraint, outer field lines would stretch faster than inner lines (at large r, stretching at a speed > c except for inertia in the relativistic momentum equation). That there is a constraint is shown by adding up the δK's to obtain the total helicity which must not exceed the source. I have done this using energy instead, giving the lnR/a in inductance if the dynamics creates a blunt nose, as contended in our paper.

2. Time-Dependent Grad-Shafranov (GS) Equation

The momentum equation when mass is conserved is:

$\rho[\partial\mathbf{v}/\partial t + (\mathbf{v}\cdot\nabla)\mathbf{v}] \; = \; \mathbf{F} \; + \mathbf{j} \times \mathbf{B} \; - \nabla p$

where **F** is gravity etc. The standard Grad-Shafranov Eq. in 2D cylinder geometry is:

$\mathbf{j} \times \mathbf{B} \quad = \quad (\Delta^*\psi)\nabla\psi + I^*\partial I^*/\partial\psi = \quad (dp/d\psi)\nabla\psi,\; I^* = rB_\phi\,,\; \psi = rA_\phi$ (no 2π)

$\Delta^*\psi \quad = \quad r\partial/\partial r\,(r^{-1}\partial\psi/\partial r) \; + \quad \partial^2\psi/\partial z^2$

The term $\rho\partial\mathbf{v}/\partial t$ can be approximated as, keeping only E_ϕ:

$\mathbf{v} \quad = \quad c(\mathbf{E}\times\mathbf{B}/B^2) \; = \; - \; (r^{-1}\partial\psi/\partial t)(\underline{\phi}\times\mathbf{B}_{POL}/B^2) \; = \quad (r^{-1}\partial\psi/\partial t/B^2)\,\nabla\psi$

$\rho\partial\mathbf{v}/\partial t \; = \; - \rho\partial/\partial t\,(r^{-1}\partial\psi/\partial t/B^2)\,\nabla\psi \; \approx \; - (1/4\pi v_A^{\,2})\partial^2\psi/\partial t^2$

Then the approximate time-dependent GS equation is, omitting $(\mathbf{v}\cdot\nabla)\mathbf{v}$:

$(1/4\pi v_A^2)\partial^2\psi/\partial t^2 = (\Delta^*\psi)\nabla\psi + I\partial I/\partial\psi - dp/d\psi$

Together with Faraday's Law and dynamo I* from angular momentum conservation, this describes jet evolution including evolution as quasi-steady states with blunted nose since $v_A >> dL/dt$.

3. GS equation in Corsica: $I^*\partial I^*/\partial\psi = \lambda \int_0^\psi \partial\psi\, \lambda$

Using $(4\pi/c)\mathbf{j} = \lambda\mathbf{B}$, for p = 0 we can write:

$I^* = \int_0^r rdr(4\pi j_z/c) = \int_0^r rdr\, \lambda B_z = \int_0^r rdr\, \lambda\, (r^{-1}\partial\psi/\partial r) = \int_0^\psi \partial\psi\, \lambda$

For open line boundary condition, $-\lambda \int_0^\psi \partial\psi\, \lambda$ includes the dynamo through $(2\pi I^* B_z/c) = [2\pi \int_0^\psi d\psi\, \lambda)\, B_z/c] = M^* r^{-1}\partial/\partial r\, (r^2\Omega)$

Code failure:

We are using Corsica in the "spheromak mode" giving a closed spheromak. This determines the field topology required, this mode being one with a magnetic axis for the closed surfaces around $r \approx R/2$ and z = 0 for a cylindrical flux conserver radius R, z (we are taking boundary at r = R = 60, z = L = 240). There also may be "private flux" near the bottom where the accretion disk dynamo attaches to the flux conserver. Private flux is a failure of "bubbleburst" in that region.

The condition for flux closure in the main volume of the flux conserver is that the bias field from the disk cancel the fringe field $(4\pi\Delta I_\psi/cL)$ due to ΔI_ψ inside the closed spheromak, at a distance D < R/2, this being the radius of the fringe field. Taking a dipole approximation to the field of radius R_o (the O-point radius of the disk), the condition is:

$$B_0\, (R_o/D)^3 = (4\pi\Delta I_\psi/cL)$$

We can express the peak bias field B_0 in terms of the total I_ψ in the flux conserver using:

$$(I_\psi/L) = \int_0^R drj_\psi = \int_0^R dr(c/4\pi)(-\partial B_z/\partial r) = (c/4\pi)B_z(0) \approx (c/4\pi C)B_o$$

where C is the ratio of B(0) at z = 0 to that at z = 120 midway up the flux conserver. Then achieving D < R/2 requires:

$$(\Delta I_\phi/I_\phi) \quad > \quad C\,(2R_o/R)^3$$

This is marginally satisfied for our accretion disk which should achieve straight flux surfaces giving C = 1 since in Section 3 we found $(\Delta I_\phi/I_\phi) \approx \delta B/B \approx 10^{-6}$ and in Section 5 $(R/R_o) \approx (1/3L/R_o) \approx 30$. Hence we are correct in seeking the closed surface solution from Corsica.

Appendix C

Eq. (C1) Collisional resistivity is negligible, giving a current/field diffusion coefficient and diffusion time t:

$$D = (\eta c^2/4\pi) = [1.3 \times 10^{-3}\, T_{eV}^{-3/2}/(\mu_o=(4\pi/10^7)]_{MKS} \times 10^4$$
$$= 1.04\times10^7\, T_{eV}^{-3/2}\ cm^2/s$$
$$t = H^2/D = [(.46 \times 3 \times 10^{14})^2(r/a)]/[1.04\times10^7\, T_{eV}^{-3/2}]$$
$$= 1.8 \times 10^{21}\,(r/a)\, T_{eV}^{3/2} > \tau >> \Omega^{-1} = 0.5 \times 10^5\,(a/r)^{3/2}$$

Eq. (C2 – C8) MRI scaling, keeps only v_ϕ, constant B_z to lowest order, ϕ and r components of perturbations $\mathbf{v}_1$ and $\mathbf{B}_1$ to first order, v_r to second order to obtain accretion. Linearized Faraday's Law and dispersion relation from Ref. [29]

$$\underline{\mathbf{r}}\,(E_r + c^{-1} v_\phi B_z) + c^{-1}\,[\,\underline{\phi}\,\langle v_{2r}\rangle B_z + \langle \mathbf{v}_1 \times \mathbf{B}_1\rangle] = 0 \qquad (C1)$$

Setting the $\underline{\mathbf{r}}$ term equal zero givers the zero order dynamo electric field. Setting the term in […] equal zero gives the accretion velocity due to turbulence as discussed below. Perturbations are:

First order

$$\partial B_{1r}/\partial t = \quad -i\omega B_{1r} = [\nabla \times (\mathbf{v}_1 \times \mathbf{B}_z)]_r \quad = \quad -ik_z\,(-v_{1r}B_z)_\phi$$
$$\partial B_{1\phi}/\partial t = \quad -i\omega B_{1\phi} = [\nabla \times (\mathbf{v}_1 \times \mathbf{B}_z)]_\phi \quad = \quad ik_z\,(v_{1\phi}B_z)_r$$

$$v_{1r} = -(\omega/k_z)(B_{1r}/B_z) \qquad (C2)$$

$$v_{1\phi} = -(\omega/k_z)(B_{1\phi}/B_z) \qquad \text{(C3)}$$

Next order (involving $\partial/\partial r$): In the $\partial B_{1\phi}/\partial t$ equation, having set the zero order terms equal to zero, additional terms give:

$$ik_z(-v_{1z}B_\phi)_r - \partial/\partial r\,(v_{1r}B_\phi)_z = 0 \qquad \text{(C6)}$$

In the z equation omitted in the MRI dispersion relation:

$\partial B_{1z}/\partial t = -i\omega B_{1z} = \partial/\partial r\,(-v_{1r}B_z)_\phi$.

These expressions yield:

$$B_{1z} = -(i\omega)^{-1}\partial/\partial r\,(-v_{1r}B_z) \qquad \text{(C7)}$$

$$v_{1z} = -(ik_zB_\phi)^{-1}\partial/\partial r\,(v_{1r}B_\phi) \qquad \text{(C8)}$$

MRI Transport, using Eqs. (C2,C3,C7,C8):

Accretion velocity

Having set $-\partial A_\phi/\partial t = 0$ (steady state) in Eq. (C1) and also having set the zero order radial terms in equal to zero (giving the dynamo electric field), we now set the remaining azimuthal term […] equal zero, giving:

$$-\langle v_{2r}\rangle B_z + \langle(v_{1z}B_{1r} - v_{1r}B_{1z})\rangle_\phi = 0 \qquad (*)$$

$$v_{1z}B_{1r} = -(B_{1r}/ik_zB_\phi)\,\partial/\partial r\,(v_{1r}B_\phi) = -(B_{1r}/ik_z)[\partial v_{1r}/\partial r + v_{1r}(B_\phi^{-1}\partial B_\phi/\partial r)]$$

$$-v_{1r}B_{1z} = (\omega/k_z)(B_{1r}/B_z)(1/i\omega)\partial/\partial r(v_{1r}B_z) = (B_{1r}/ik_z)[\,[\partial v_{1r}/\partial r + v_{1r}(B_z^{-1}\partial B_z/\partial r)]$$

Adding and introducing the result into the $\langle v_{2r}\rangle$ equation above gives:

$$v_r \equiv \langle v_{2r}\rangle = B_z^{-1}\,\mathrm{Re}\{v_{1r}(B_{1r}/ik_z)\,[-(B_\phi^{-1}\partial B_\phi/\partial r) + (B_z^{-1}\partial B_z/\partial r)]\}$$

$$v_r = -(3/2 - 1)(\omega/k_z^2 r)(B_{1r}/B_z)^2 = 1/2\,(\Omega/k_z^2 r)(B_{1r}/B_z)^2 \qquad \text{(C9)}$$

Here we use the asymptotic results $(B_z^{-1}\partial B_z/\partial r) = -3/2$ and $(B_\phi^{-1}\partial B_\phi/\partial r) = -1$, and we use Eq. (C2) to obtain $v_{1r} = -(\omega/k_z)(B_{1r}/B_z) = (\Omega/k_z)(B_{1r}/B_z)$ where $\Omega < 0$ by our convention giving also an accretion velocity $v_r < 0$ as it should be.

Axial pressure due to turbulence

Using Eq. (C8), we take:

$v_{1z} = \mathrm{Re}\,(ik_z B_\phi)^{-1}\partial/\partial r\,(v_{1r}B_\phi) \approx (1/k_z r)v_{1r} = (\omega/k_z^2 r)(B_{1r}/B_z)$

$P_z = 1/2\,\rho v_{1z}^2 = 1/2\,\rho[(\omega/k_z^2 r)(B_{1r}/B_z)]^2$

Using v_r above and Eq. (A8) giving $M^* = -2\pi r\Sigma v_r = -2\pi r\rho H v_r$ and $k_z = \pi/H$ we obtain, for negative Ω:

$$P_z = -\rho\omega r\,(1/k_z r)^2[1/2\,(\omega/k_z^2 r)(B_{1r}/B_z)^2]$$
$$= -\rho\omega r v_r\,(1/k_z r)^2$$
$$= -\alpha_z\Omega(2\pi r H\rho v_r/2\pi r H)(H^2/r) = -\alpha_z(\Omega M^*/2\pi r)(H/r) \qquad \text{(C10)}$$

where $\alpha_z = (\omega\Omega/k_z^2 H^2)$.

Hyper-resistive heating

$P_{HEAT} = j_z E_z + j_\phi E_\phi$

$-cE_z = [v_{1r}B_{1\phi} - v_{1\phi}B_{1r}]$

$= [-(\omega/k_z)(B_{1r}B_{1\phi}/B_z) + (\omega/k_z)(B_{1\phi}B_{1r}/B_z)] = 0$

$-cE_\phi = [v_{1z}B_{1r} - v_{1r}B_{1z}] = (v_r B_z)$ from (*) above

$P_{HEAT} = -c^{-1} j_\phi(-cE_\phi)$

$= (1/4\pi)(\partial B_z/\partial r)(v_r B_z) = v_r\,\partial(B_z^2/8\pi)/\partial r \qquad \text{(C11)}$

MRI Torque: $-rj_{r1}B_{1z}$ Additive to 2D counterpart, both serving to extract energy from rotation. Magnitude of fluctuations, Eqs. (C12) – (C15): see text

FIGURE CAPTIONS

Figure 1:

Snapshot sketch of current paths in a jet/radiolobe stucture ejected from an accretion disk dynamo, showing the advancing "nose" of the jet where cosmic rays are accelerated.

Figure 2:

Sketch of current paths in a spheromak plasma created by a homopolar generator, analogous to the accretion disk dynamo and jet structure in Figure 1.

Figure 3:

Predicted radial magnetic profiles in an accretion disk dynamo, showing the poloidal field B_z, the toroidal field $B_\phi = (2I(r)/cr)$ and the z-current $I(r) = \int_0^r 2\pi r dr j_z$ within a radius r. Note that **B** asymptotes to $B_\phi \propto (1/r) >> B_z \propto (1/r^{3/2})$ used to calculate the inductance in Section 2 and $E_r \propto (1/r)$ that accelerates cosmic rays in the "nose" of Figure 1.

Figure 4:

Equilibrium solution of $\nabla x \mathbf{B} = \lambda \mathbf{B}$ inside the return current boundary of Figure 1 using the Corsica code [35]. In Figure 4a, the poloidal flux $\psi(r,0)$ at z = 0 and $\lambda(\psi) \propto (j_z/B_z)$ approximate the accretion disk fields of Figure 3. Figure 4b shows j_z, λ and ψ profiles at the halfway point, z = 120.

Figure 5:

Taken from MHD simulations of jet ejection from an accretion disk, Ref. [10], showing the "mean-field" cross-section of flux surfaces in (a), the underlying 3D field lines in (b), and the mean field $B_\phi(r)$ in (c) approximating the asymptotic form $\propto 1/r$ in Figure 3.

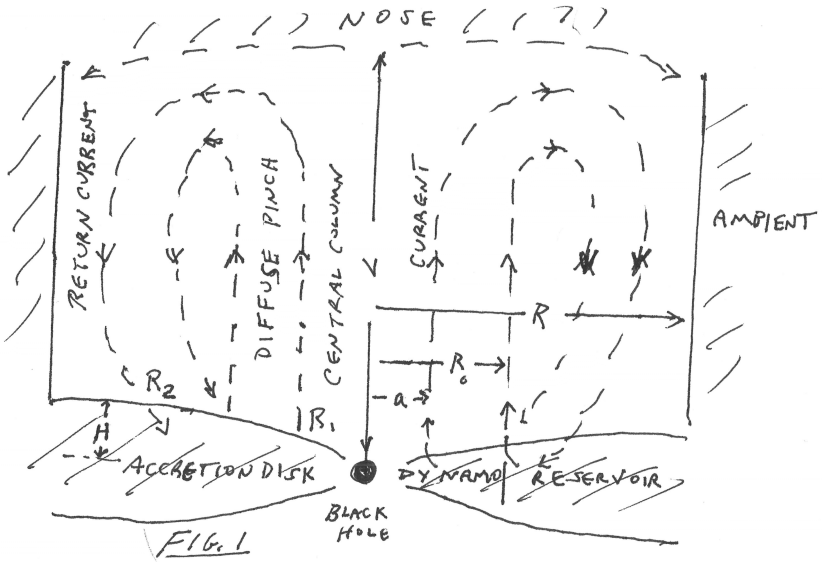
NOSE
RETURN CURRENT
DIFFUSE PINCH
CENTRAL COLUMN
CURRENT
AMBIENT
R
R_0
R_2
R_1
a
L
H
ACCRETION DISK
DYNAMO
RESERVOIR
BLACK HOLE

FIG. 1

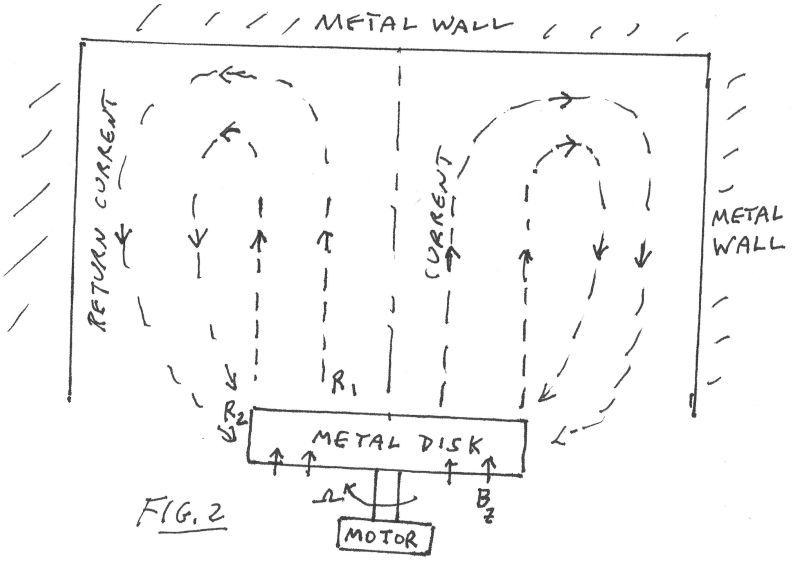
METAL WALL
RETURN CURRENT
CURRENT
METAL WALL
R_1
R_2
METAL DISK
K
B_z
MOTOR

FIG. 2

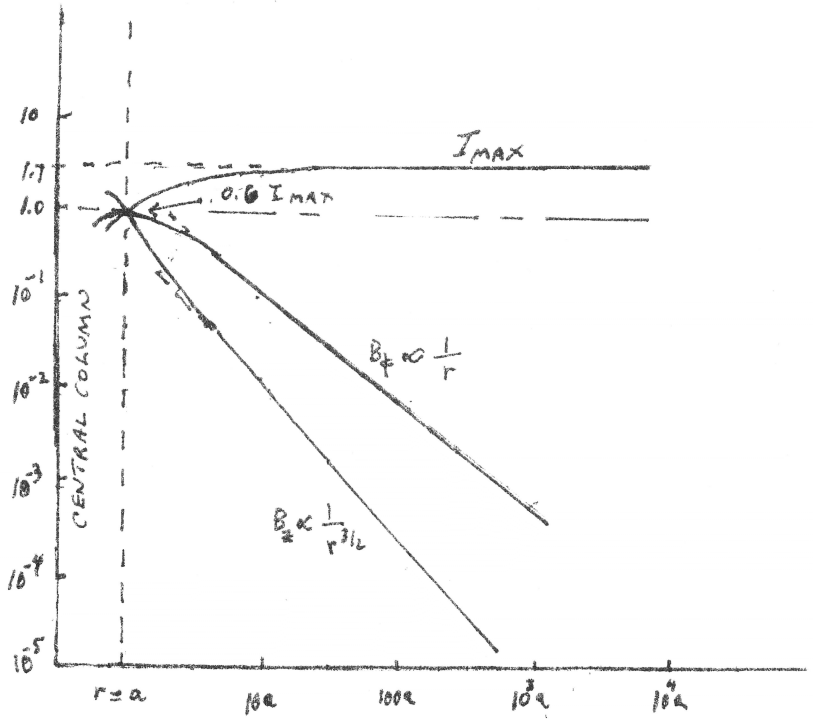
10
1.7
1.0
10^{-1}
10^{-2}
10^{-3}
10^{-4}
10^{-5}
CENTRAL COLUMN
I_{MAX}
0.6 I_{MAX}
$B_\phi \propto \frac{1}{r}$
$B_z \propto \frac{1}{r^{3/2}}$
r = a
10a
100a
10^3a
10^4a

Figure 3

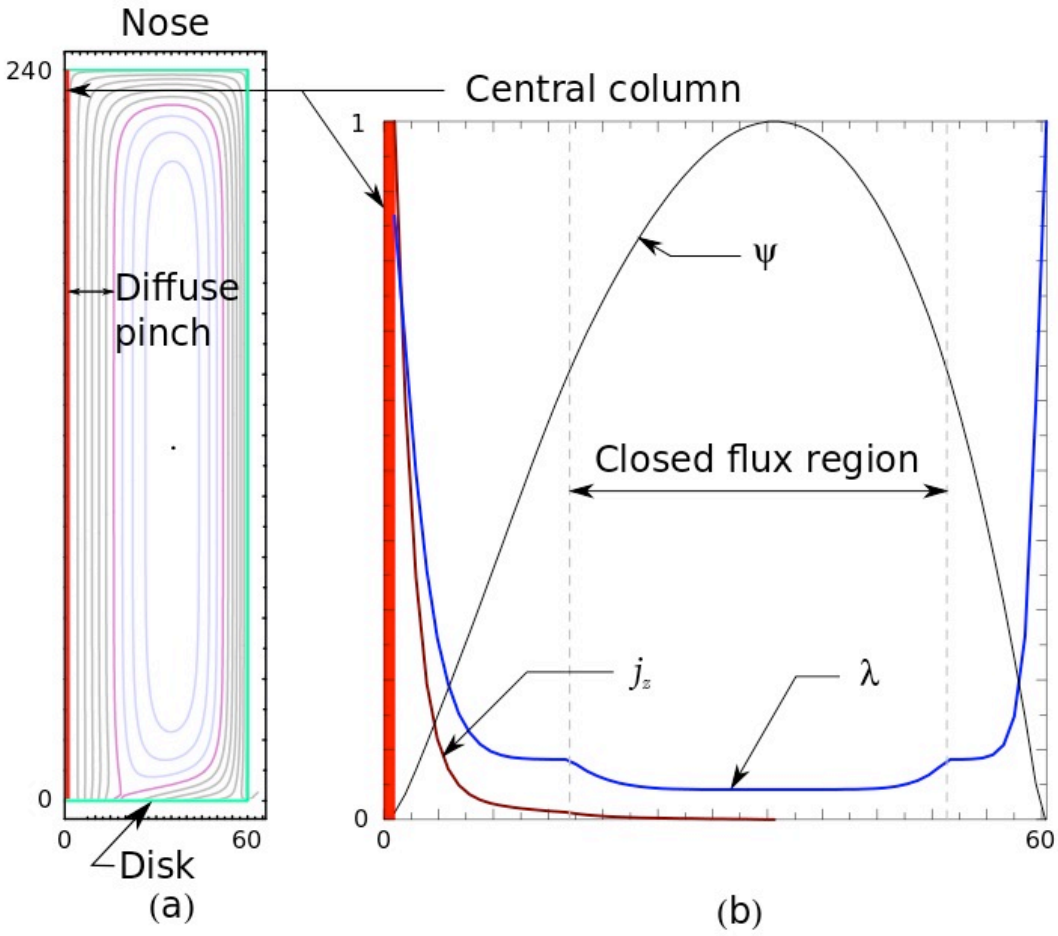
Nose
240
Central column
1
Diffuse
pinch
ψ
Closed flux region
j_z
λ
0
0
60
Disk
(a)
0
60
(b)

Figure 4

Figure 5

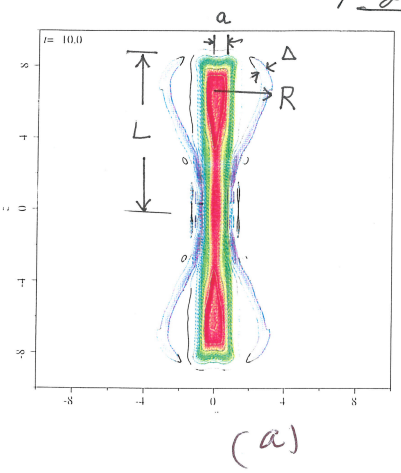

(a)

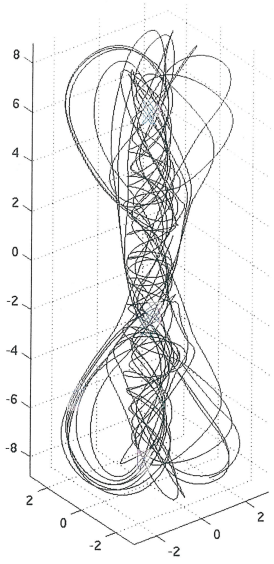

(b)

T. K. Fowler 10/1/08

Figs. 4, 3, 11 Nakamura, Li, Li,
Astrophys. J. **652**, 1059 (2006)

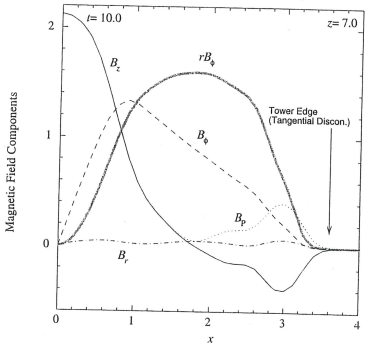

(c)

Expansion

$V = \Omega\psi$, $I = \psi/a$, $\psi = \pi a^2 B_z$

$dL/dt = (\Omega a/\ln R/a)$

Current-Limited Density

$n = (j/ec)$, $j = (I/A)$, $A = \pi a^2 \rightarrow 2\pi r\Delta$

Synchrotron radiation, central column

$I\,\delta V \propto \mathrm{Ln}(\gamma B_z)^2 \propto I\,L(\gamma B_z)^2$, $\delta V/L = -\langle vxB\rangle$

Example (MKS)

$V = 3 \times 10^{19}$ = cosmic ray, $I = 2.5 \times 10^{18}$

$a = 10^{12}$, $L = 10^{22}$

$a\Omega = 0.2\ c$, $\tau = 10^8$ yrs

$IV\tau = 2 \times 10^{53} = 2 \times 10^{60}$ ergs

$B_z = 0.5$, $\lambda = 2$ cm, $\gamma_e \approx 1$

$\delta V = 0.03$ V

Cosmic Ray Acceleration, flux return

$\Delta \rightarrow$ Larmor radius

$E_r = (V/ r \ln R/a)$

$j_r = -D(dn/dr)$, $D \approx c\Delta$ (drift cyclotron)

$N(E) \propto E^{-\Gamma}$